Monthly Notices of the ROYAL ASTRONOMICAL SOCIETY

MNRAS **545,** 1–18 (2026) https://doi.org/10.1093/mnras/staf2030
Advance Access publication 2025 November 29

A 34.6-d transiting sub-Neptune in the TOI-1422 planetary system

L. Naponiello [1]★ P. Leonardi,[2,3] M. Damasso,[1] M.-L. Steinmeyer [4] M. Stalport,[5,6] C. Dorn,[4] A. S. Bonomo,[1] L. Mancini [1,7,8] A. Sozzetti [1] S. Benatti,[9] S. Colombo[9] and R. Cosentino[10]

[1]*INAF – Osservatorio Astrofisico di Torino, Via Osservatorio 20, I-10025 Pino Torinese, Italy*
[2]*Dipartimento di Fisica, Università di Trento, Via Sommarive 14, I-38123 Povo, Italy*
[3]*Dipartimento di Fisica e Astronomia, Università degli Studi di Padova, Vicolo dell'Osservatorio 3, I-35122 Padova, Italy*
[4]*Institute for Particle Physics and Astrophysics, ETH Zürich, Otto-Stern-Weg 5, CH-8093 Zürich, Switzerland*
[5]*Space sciences, Technologies and Astrophysics Research (STAR) Institute, Université de Liège, Allée du 6 Août 19C, B-4000 Liège, Belgium*
[6]*Astrobiology Research Unit, Université de Liège, Allée du 6 Août 19C, B-4000 Liège, Belgium*
[7]*Department of Physics, University of Rome 'Tor Vergata', Via della Ricerca Scientifica 1, I-00133 Rome, Italy*
[8]*Max Planck Institute for Astronomy, Königstuhl 17, D-69117 Heidelberg, Germany*
[9]*INAF – Osservatorio Astronomico di Palermo, Piazza del Parlamento 1, I-90134 Palermo, Italy*
[10]*Fundación Galileo Galilei – INAF, Rambla José Ana Fernandez Pérez 7, E-38712 Breña Baja, TF, Spain*

Accepted 2025 November 14. Received 2025 November 13; in original form 2025 September 4

ABSTRACT

TOI-1422 is a G2 V star ($V = 10.6$ mag) known to host a warm Neptune-sized planet, TOI-1422 b, with a mass and radius of about 9 $M_\oplus$ and 4 $R_\oplus$, on a circular orbit with a period of 12.997 d. An outer planetary candidate in this system had previously been suggested on the basis of a residual signal in the radial velocity (RV) data with a tentative period of ∼29 d, along with a possible single transit-like event, although it was not clear at the time whether the two signals belonged to the same companion. In this work, we confirm the presence of a second transiting planet, TOI-1422 c, a sub-Neptune ($R = 2.61 \pm 0.14\ R_\oplus$) that orbits with a longer period of 34.563 d. This confirmation is based on the detection of three *TESS* (Transiting Exoplanet Survey Satellite) transits, two from newly available sectors, combined with new and archival RV measurements. The sub-Neptune ($\rho_c = 4.3^{+1.3}_{-1.0}$ g cm^{-3}) is more massive than the inner Neptune ($\rho_b = 0.93^{+0.21}_{-0.20}$ g cm^{-3}), having a mass of $M_c = 14 \pm 3\ M_\oplus$, making TOI-1422 a rare anti-ordered system. Furthermore, we detect transit timing variations (TTVs) on the inner planet, with amplitudes of up to 5 h, suggesting ongoing dynamical interactions. A dynamical analysis that combined TTVs and RVs indicates that planet c alone is unlikely to account for the full TTV amplitude observed on TOI-1422 b. We investigated whether an additional, as yet undetected companion could account for the observed signal, exploring a range of plausible orbital configurations and finding that a low-mass planet located between the two known orbits may be responsible.

Key words: methods: data analysis – techniques: photometric – techniques: radial velocities – planets and satellites: detection – planets and satellites: dynamical evolution and stability – planets and satellites: fundamental parameters.

1 INTRODUCTION

The architectural arrangement of planets within a single system provides one of the most stringent tests of planet formation theory. While the properties of an individual planet constrain its nature, the relative ordering of masses and radii among sibling planets acts as a direct fossil record of their collective origin and evolution (J. N. Winn & D. C. Fabrycky 2015). From this comparative approach, two general features have emerged for mature systems: (i) an intra-system uniformity known as 'peas in a pod', i.e. planets in the same system tend to be similar in size and regularly spaced (S. Chatterjee & J. C. Tan 2014; S. Millholland, S. Wang & G. Laughlin 2017; L. M. Weiss et al. 2018), and (ii) a predictable (non-linear) mass–radius relation where larger planets are also more massive (J. J. Fortney, M. S. Marley & J. W. Barnes 2007; E. D. Lopez & J. J. Fortney 2014; J. Chen & D. Kipping 2017). Systems that violate these general patterns offer invaluable clues about the non-canonical, often extreme, processes that shape planetary architectures. A notable exception to the aforementioned trends occurs in the small subset of multiplanet systems where the inner planet is substantially larger in size but less massive than its companion on a wider orbit (see e.g. the list compiled by A. R. Howe et al. 2025).

A particular case is that of the two warm mini-Neptunes in the TOI-815 system (A. Psaridi et al. 2024), where the inner planet, TOI-815 b, has both a larger radius and a lower mass than the outer planet TOI-815 c. This configuration presents a challenge to quiescent formation models, which struggle to explain how a smaller, denser, and more massive body could form or end up in an orbit exterior to a larger, less massive 'puffy' sibling. Explaining this configuration points towards a more dynamic formation history than is typically assumed. The observed architecture could be the

★ E-mail: luca.naponiello@inaf.it

result of gravitational scattering events that re-ordered the system, transporting planets from different birth locations (A. Izidoro et al. 2015; B. Bitsch et al. 2019). Alternatively, the outer planet may have suffered a catastrophic giant impact late in its evolution, which would have stripped away a primordial gas envelope, leaving behind a smaller, denser, and now more massive core (S.-F. Liu et al. 2015; A. S. Bonomo et al. 2019; A. Psaridi et al. 2024). Both scenarios imply a departure from the smooth processes that are believed to shape most of planetary systems.

In this paper, we report the discovery of a second transiting planet orbiting TOI-1422, a quiet G2 V star ($V = 10.6$ mag) 155 pc away, previously known to host a warm Neptune-sized planet ($P_{\rm orb} = 12.997$ d; L. Naponiello et al. 2022). The new planet, a sub-Neptune, orbits externally to the first and is smaller in size, yet our analysis reveals that it is the more massive of the two. Furthermore, significant transit timing variations (TTVs) detected for the inner planet, unrelated to the new one, suggest that the system is not yet fully characterized and may host an additional unseen perturber. The system therefore represents a compelling natural laboratory for studying complex evolutionary histories of exoplanets.

The paper is structured as follows. In Section 2, we describe the new photometric and spectroscopic observations. In Section 3, we present the system parameters derived from our global analysis that confirm this unusual hierarchy. We explore the composition of both planets in Section 4, discuss the properties of the system in Section 5, and draw conclusions in Section 6.

2 OBSERVATIONS AND DATA REDUCTION

2.1 *TESS* photometry

TIC 333473672 (TOI-1422) has been observed by *TESS* (Transiting Exoplanet Survey Satellite) in late 2019 (Sectors 16 and 17), in October 2022 (Sector 57), and, recently, in October 2024 (Sector 84). We retrieved the 2-min cadence photometry of all four sectors from the Mikulski Archive for Space Telescopes (MAST), as reduced by the Science Processing Operations Center (SPOC; J. M. Jenkins et al. 2016) pipeline, developed at the NASA Ames Research Center. In particular, we used the Presearch Data Conditioning Simple Aperture Photometry (PDC-SAP; J. C. Smith et al. 2012; M. C. Stumpe et al. 2012, 2014) light curve, which is already corrected for dilution and systematics. We found no appreciable short- or long-term modulation in both the PDC-SAP and SAP light curves, in accordance with the notion that the star is rather old and quiet (L. Naponiello et al. 2022).

2.2 Radial velocities

The original radial velocity (RV) data set was obtained from 112 spectra taken with the High Accuracy Radial velocity Planet Searcher for the Northern hemisphere (HARPS-N; R. Cosentino et al. 2012) instrument at the Telescopio Nazionale Galileo (TNG) in La Palma (Spain), within the GAPS (Global Architecture of Planetary Systems) Neptune programme (L. Naponiello et al. 2022).On top of that, we included nine new spectra recently taken with the same instrument, as part of the 'Ariel Masses Survey (ArMS)' large programme (Di Maio et al., in preparation), dedicated to the precise mass measurement of transiting planets with radii spanning the radius valley potentially valuable for atmospheric characterization with the European Space Agency (ESA) Mission Ariel (G. Tinetti et al. 2018).The new observations were carried out to refine the ephemerides of TOI-1422 b, which is considered a promising Ariel target with a transmission spectroscopy metric of ∼100, and to investigate the origin of the linear trend reported in L. Naponiello et al. (2022).

The RVs and activity indices (Table B1) were extracted using version 3.0.1 of the HARPS-N Data Reduction Software (DRS; X. Dumusque et al. 2021). In total, after removing one outlier,[1] we used 120 RVs with an average uncertainty of 3.0 m s^{-1}, a weighted root-mean-square (wrms) of ∼5 m s^{-1}, and a signal-to-noise ratio (SNR) of ≈45, measured at a reference wavelength of 5500 Å. Recently, 34 RV measurements of TOI-1422, with an average uncertainty of 2.1 m s^{-1} (but with a large wrms of ∼7 m s^{-1}), were released (A. S. Polanski et al. 2024). However, we did not include the RVs obtained by the High Resolution Echelle Spectrometer (S. S. Vogt et al. 1994) in this work due to their limited number and sparse temporal sampling (one observation every ∼28 d).

The updated HARPS-N RV data set now reveals a quadratic trend extending beyond the observational time span (∼1700 d), although it could be stellar in origin as it closely resembles the shape of two activity indicators (see Figs A1 and A2), despite the star being rather quiet, with a median chromospheric index of $\log R'_{\rm HK} = -4.942 \pm 0.005$. While we refer to the discovery paper (L. Naponiello et al. 2022) for a careful analysis of the activity diagnostics (the new data set only includes nine new RVs taken a few years later), we report in Fig. A3 the generalized Lomb–Scargle (GLS) periodograms of the $\log R'_{\rm HK}$ and Hα indices, which show a long-term modulation similar to that of the RVs.

We treated this trend employing a simple quadratic term in the global analysis that follows (see Section 3.3), rather than using a Gaussian process (GP; V. Rajpaul et al. 2015). The long-term variation is well defined and could also arise from a combination of stellar activity and a genuine long-period planetary signal, so we considered it safer and more transparent to model it as a deterministic trend, especially since GPs can be overly flexible and partially absorb low-amplitude planetary signals (e.g. S. Blunt et al. 2023).

3 ANALYSIS

3.1 GLS periodogram

We computed the GLS periodogram for the HARPS-N residual RVs, after removing both the long quadratic term and the TOI-1422 b signal. We found that the highest power does not correspond to ∼29 d, the signal announced by L. Naponiello et al. (2022), but rather to ∼34.6 d, one of the two aliases indicated in fig. D2 of the same paper, with a low false alarm probability (FAP) of 0.2 per cent (Fig. 1). However, these two signals are easily recognized as aliases of each other when combined with the second highest frequency of the window function (1/190 d) between 1.5 and 1000 d. Therefore, this information alone is not sufficient to determine whether one of these signals is of planetary origin, nor to establish which one is genuine.

3.2 Photometric periodograms

A single transit-like signal, which meets the minimum diagnostic criteria,[2] was first reported in the discovery paper near

[1] This RV point has the largest uncertainty (∼9 m s^{-1}) and corresponds to the spectrum with the lowest SNR of our data set, which also yields anomalous values in all the activity indices.

[2] In particular, the event was transit-shaped with resolved ingress and egress, showing no correlation with the X–Y pixel position or background flux, and

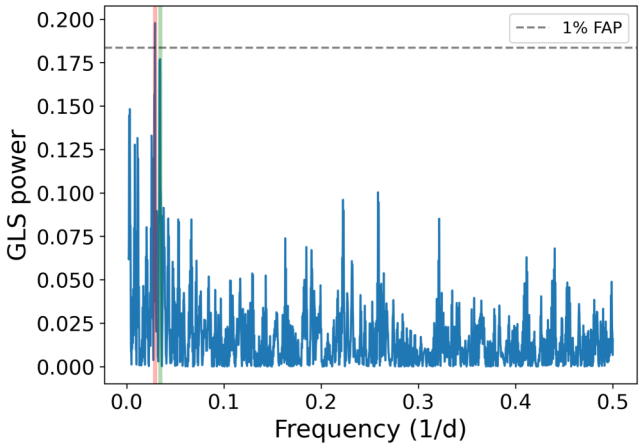

Figure 1. GLS periodogram of the RV residuals from the one-planet model, once the quadratic trend has been removed. The vertical lines signal, respectively, the periodicity of 34.6 (first peak) and 29.0 d (second peak), while the horizontal dashed line marks the 1 per cent FAP.

2458756.35 BJD_{TDB}, yet the authors argued that it was not compatible with the 29-d RV signal as 'the lack of other transits in the *TESS* light curve suggests an orbital period between 17 and 22, or longer than∼35 d'. With the addition of two *TESS* sectors and the 34.6-d signal gaining ground over the 29-d one in the new RV data set, we searched the entire TOI-1422 light curve for new transits using the Cambridge Exoplanet Transit Recovery Algorithm (L. C. Smith et al. 2025), a fast and sensitive transit detection algorithm optimized for graphic processing units. In particular, after masking TOI-1422 b transits, we have searched for transits with a minimum depth of 50 parts per million (ppm).

The algorithm identified a peak with a period of 34.56 d, corresponding to a transit duration of 6.9 h, a transit depth of 683 ± 48 ppm, and an SNR $\sim$ 14.3, with the centre of the first transit being pinpointed at 2458756.367 BJD_{TDB}, precisely matching the single transit previously reported. We repeated the analysis using the more commonly used box least-squares (G. Kovács, S. Zucker & T. Mazeh 2002) and transit least-squares (M. Hippke & R. Heller 2019) periodograms, finding the same periodicity, although with lower significance. In total, three transits have been observed for this new candidate, one for each *TESS* sector, with the exclusion of Sector 17. For TOI-1422 b, the number of transits amounts to 7 at the time of writing, compared to 4 of the discovery paper. The host star is not scheduled for observation by *TESS* in the upcoming sectors.

3.3 Global fit

For homogeneity with the previous work, we have performed a joint transit and RV analysis employing `juliet` (N. Espinoza, D. Kossakowski & R. Brahm 2019) and using the same approach described by L. Naponiello et al. (2022). Mainly, we have tried different models with a combination of one or two planets and fixed to zero or free eccentricities. We found that the two-planet model with circular orbits is more significant than the two-planet model with free eccentricities ($\Delta \ln \mathcal{Z}^{e=0}_{e\geq 0} = 6.9$), which, at the same time, is much more significant than any one-planet model ($\Delta \ln \mathcal{Z}^{2p}_{1p} > 10$, where $\mathcal{Z}$ is the Bayesian evidence of each fit). Therefore, we consider TOI-1422 c as a new confirmed planet with $P_{orb} = 34.5633 \pm 0.0002$ d, $M_c = 14 \pm 3$ $M_\oplus$, and $R_c = 2.61 \pm 0.14$ $R_\oplus$. The phased RV signal and the transits of TOI-1422 c have been plotted in Fig. 2, while in Fig. A4 we show the entire RV data set. We also refined the parameters of TOI-1422 b (see Table 1), which are mostly in agreement with the previous estimates.

Finally, the GLS periodogram of the adopted model's residuals (Fig. A5) reveals a signal at about 387 d (FAP $\lesssim 1$ per cent). However, a subsequent three-planet model failed to properly account for this signal, and we therefore do not consider it significant. We stress that this signal's origin is unclear: while it is close to the possible 1-yr Earth alias, it also corresponds to a potential periodicity found in our dynamical analysis (Section 3.5).

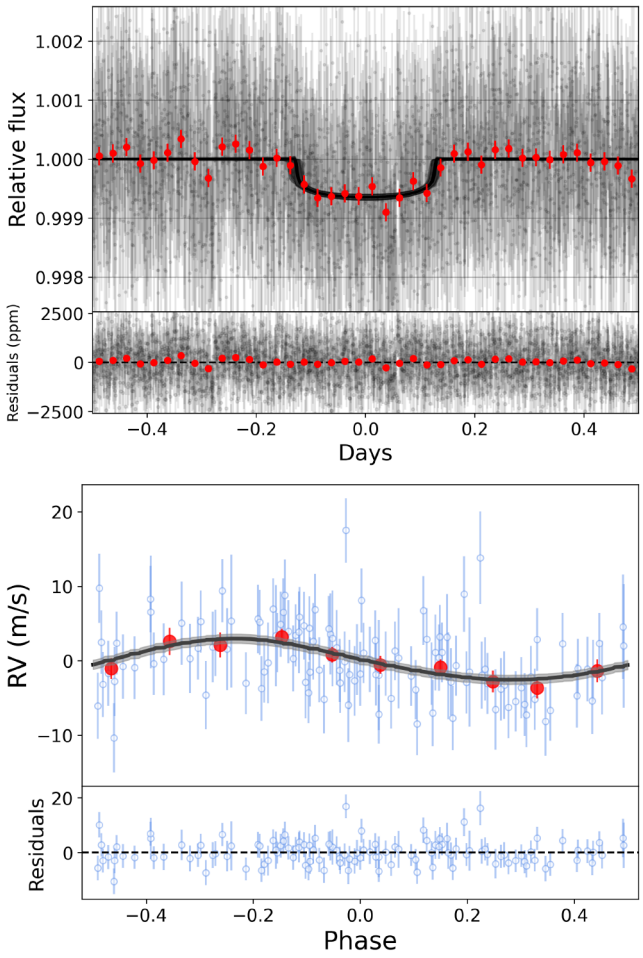

Figure 2. Phased *TESS* transits (top panel) and RV signal (bottom panel) of TOI-1422 c, along with the best-fitting models and their residuals below each panel. The large circles represent the average of ∼31 min and ∼83 h, respectively, while the shaded areas represent the 1σ deviation from each model.

3.4 Transit timing variations

In an isolated Keplerian system, planetary transits occur with clockwork regularity. Any significant deviation from this periodicity (TTVs) indicates the presence of additional dynamical or physical processes at play. Such variations are most often driven by gravi-

exhibiting a consistent depth across different photometric apertures. The signal was also recovered independently with multiple photometric pipelines, including those employing alternative neighbour-subtraction techniques (L. Naponiello et al. 2022).

Table 1. Priors and posteriors for the global analysis of TOI-1422. Priors are listed for fitted parameters, while derived parameters are calculated from the posteriors of the fitted model.

	Prior	TOI-1422 b		TOI-1422 c
Stellar parameters				
Stellar density, $\rho_\star$ (kg m^{-3})	$\mathcal{N}(1300,\ 100)$[a]		1277 ± 88	
Systemic velocity, γ (m s^{-1})	$\mathcal{U}(-25\,957,\ -25\,937)$		$-25\,948^{+7}_{-6}$	
Transit and orbital parameters				
Orbital period, $P_{\rm orb}$ (d)	$\mathcal{N}(12.99, 0.01)$ (b) $\mathcal{U}(15, 100)$ (c)	$12.998\,94 \pm 0.000\,03$		34.5633 ± 0.0002
Time of transit, T_0 (BJD−2458700)	$\mathcal{N}(45.92, 0.01)$ (b) $\mathcal{N}(56.351, 0.01)$ (c)	$45.9405^{+0.0023}_{-0.0021}$		$56.3525^{+0.0062}_{-0.0057}$
RV semi-amplitude, K (m s^{-1})	$\mathcal{U}(0, 10)$	$2.64^{+0.54}_{-0.53}$		2.80 ± 0.59
r_1[b]	$\mathcal{U}(0, 1)$	0.0345 ± 0.0009		0.023 ± 0.001
r_2[b]	$\mathcal{U}(0, 1)$	0.19 ± 0.12		$0.17^{+0.14}_{-0.12}$
Eccentricity, e	Fixed at 0[d]	<0.20[f]		<0.20[f]
Argument of periastron, ω (deg)	Fixed at 90[d]	Unconstrained		Unconstrained
Parametrized limb-darkening coeff., q_1	$\mathcal{N}(0.31, 0.30)$[e]		$0.40^{+0.21}_{-0.17}$	
Parametrized limb-darkening coeff., q_2	$\mathcal{N}(0.25, 0.10)$[e]		0.25 ± 0.09	
Derived parameters				
Total transit duration, T_{14} (h)	Derived	4.46 ± 0.12		6.12 ± 0.18
Orbital inclination, i (deg)	Derived	$89.53^{+0.30}_{-0.31}$		$89.77^{+0.15}_{-0.19}$
Impact parameter, b	Derived	0.19 ± 0.12		$0.17^{+0.14}_{-0.12}$
Scaled semimajor axis, $a/R_\star$	Derived	$22.51^{+0.50}_{-0.53}$		$43.20^{+0.97}_{-1.02}$
Planet radius, $R_{\rm p}$ ($R_\oplus$)	Derived	3.83 ± 0.11		2.61 ± 0.14
Planet mass, $M_{\rm p}$ ($M_\oplus$)	Derived	$9.5^{+2.0}_{-1.9}$		14 ± 3
Planet density, $\rho_{\rm p}$ (g cm^{-3})	Derived	$0.93^{+0.21}_{-0.20}$		$4.3^{+1.3}_{-1.0}$
Equilibrium temperature, $T_{\rm eq}$[c] (K)	Derived	870 ± 14		628 ± 10
Surface gravity, log $g_{\rm p}$ (cgs)	Derived	$6.37^{+1.39}_{-1.34}$		$20.12^{+5.09}_{-4.56}$
Semimajor axis, a (au)	Derived	0.107 ± 0.003		0.205 ± 0.005
Limb-darkening coeff., u_1	Derived		$0.31^{+0.15}_{-0.13}$	
Limb-darkening coeff., u_2	Derived		$0.30^{+0.15}_{-0.13}$	
Instrumental parameters				
HARPS-N RV jitter, $\sigma_{\rm HARPS\text{-}N}$ (m s^{-1})	$\mathcal{U}(0, 10)$		3.5 ± 0.4	
RV trend coeff., A[g] (m s^{-1} d^{-1})	$\mathcal{U}(0, 0.05)$		0.024 ± 0.005	
RV trend coeff., B[g] (m s^{-1})	$\mathcal{U}(-200, 0)$		-13 ± 7	
RV trend coeff., C[g] (m s^{-1} d^{-2})	$\mathcal{U}(-0.1, 0.1)$		$(8 \pm 2) \cdot 10^{-6}$	
TESS white noise, σ_{TESS} (ppm)	$\mathcal{L}(10^{-2}, 10^2)$		$0.5^{+9.0}_{-0.5}$	
TESS GP amplitude, $\sigma_{{\rm GP},TESS}$ (ppm)	$\mathcal{L}(10^{-6}, 10)$		0.13 ± 0.02	

Table 1 – *continued*

	Prior	TOI-1422 b	TOI-1422 c
TESS GP time-scale, $\rho_{\mathrm{GP},\,TESS}$ (d)	$\mathcal{L}(10^{-2}, 10)$	$0.78^{+0.15}_{-0.20}$	

[a]We adopt the stellar density prior derived from the stellar characterization presented in L. Naponiello et al. (2022).
[b](r_1, r_2) is the parametrization described in N. Espinoza (2018) for $R_{\mathrm{p}}/R_\star$ and the impact parameter b.
[c]This is the equilibrium temperature for a zero Bond albedo and uniform heat redistribution to the nightside.
[d]In the case of non-null eccentricity, the priors were set as follows: $(\sqrt{e}\,\sin\omega, \sqrt{e}\,\cos\omega)$ in $\mathcal{U}(-1.0,\ 1.0)$.
[e]The limb-darkening priors come from the theoretical values of A. Claret (2017), following L. Naponiello et al. (2022).
[f]The eccentricity upper limit is constrained at the confidence level of 1σ.
[g]A, B, and C are coefficients of the long-term trend, which is added to the Keplerian model and is of the form $B + A(t - t_i) + C(t - t_i)^2$.

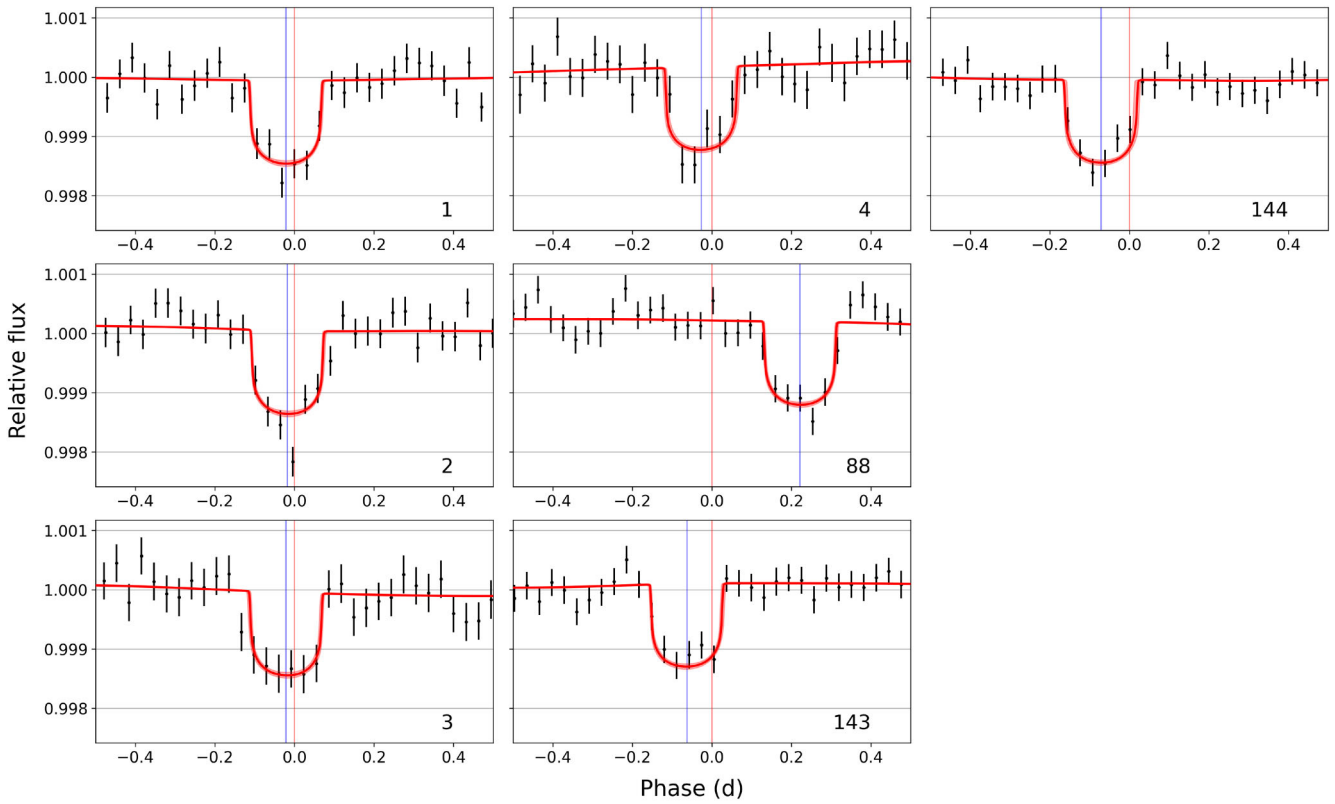

Figure 3. TTVs of TOI-1422 b. The epochs of the transits are labelled on the bottom right of each panel. The vertical lines indicate, respectively, the calculated (at phase zero) and observed centre times of the transits.

tational perturbations from other planets (E. Agol et al. 2005; M. J. Holman & N. W. Murray 2005) but can also result from secular effects acting on close-in giant planets, including tidal orbital decay (F. A. Rasio et al. 1996; K. C. Patra et al. 2017; P. Leonardi et al. 2024) or apsidal precession (D. Ragozzine & A. S. Wolf 2009).

For stars that are bright enough, it is also possible to obtain high-precision RV measurements that, combined with TTVs, allow alleviation of their individual biases and posterior degeneracies (L. Malavolta et al. 2017; D. Nespral et al. 2017; E. A. Petigura et al. 2018; V. Nascimbeni et al. 2023; L. Borsato et al. 2024; J. Korth et al. 2024).

No TTVs were detected in the discovery paper of TOI-1422 b, as only four transits of the Neptune-sized planet had been observed consecutively in *TESS* Sectors 16 and 17. In contrast, our updated analysis, benefiting from an extended time baseline, reveals a significant deviation, especially in the timing of the fifth detected transit of TOI-1422 b (epoch 88, observed in Sector 57). By fitting each mid-transit time independently (Fig. 3), we find that this transit occurs more than 8 h later than predicted by a linear ephemeris (Fig. 4). A similar analysis was performed for TOI-1422 c. However, with only three observed transits, no significant timing deviations were detected (Fig. A6). Given the separation between the planets (period ratio $P_{\mathrm{c}}/P_{\mathrm{b}} \approx 2.65$), TOI-1422 b and TOI-1422 c are not in or near a strong low-order mean motion resonance (MMR), which could help to explain the observed TTVs' amplitude. Such a large deviation therefore strongly suggests gravitational perturbations from an additional, as yet undetected, planetary companion.

3.5 Dynamical modelling: TTVs + RVs

To investigate which dynamical interactions can be responsible for the observed timing variations, we employed the *N*-body integrator

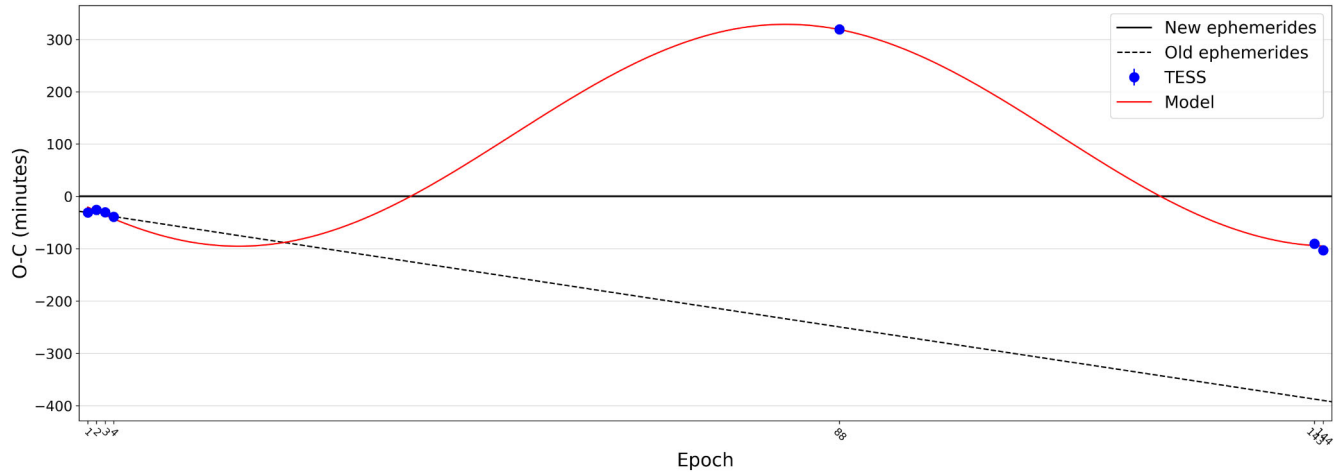

Figure 4. O − C centre times of transits for TOI-1422 b. The ephemerides published in the discovery paper are represented by the dashed line, while the solid line represents the ephemerides as evaluated in this manuscript. The curved line is a simple sinusoidal fit to the O − C times. The error bars of the O − C times are smaller than the represented circles.

included in TRADES[3] (L. Borsato et al. 2014, 2019, 2021), which simultaneously fits the transit times and RV measurements (see Table B1), while integrating the system parameters.

We tested four different dynamical configurations for the system: (1) a two-planet model including only the known transiting planets; (2) a three-planet model with an additional inner perturber interior to TOI-1422 b; (3) a three-planet model with a perturber between TOI-1422 b and TOI-1422 c; and (4) a three-planet model with an external perturber beyond TOI-1422 c. For all the configurations, we used as fitting parameters the planetary-to-star mass ratio $M_p/M_\star$, the period P_p, the eccentricity e_p, and the mean longitude λ_p.[4] To improve sampling efficiency and avoid biases at low eccentricities, we adopted the parametrization $[\sqrt{e}\cos\omega, \sqrt{e}\sin\omega]$ (J. Eastman, B. S. Gaudi & E. Agol 2013) instead of fitting the eccentricity e and the argument of the periastron ω directly. The stellar radius ($R_\star$) and the stellar mass ($M_\star$) were fixed to the values reported by L. Naponiello et al. (2022). The radii (R_p) and orbital inclinations of the two transiting planets were fixed to the values derived in Section 3.3, while the inclination of the potential third planet was treated as a free parameter of the fit. The longitude of the ascending node was fixed at $\Omega = 180°$ for planet b, while it was allowed to vary $180 \pm 10°$, for planets c and d, in line with previous works (e.g. J. N. Winn 2010; L. Borsato et al. 2014). For the RV data set, we included a jitter term $\sigma_{\rm jitter}$ (parametrized in $\log_2$) and a systemic velocity offset $\gamma_{\rm RV}$ as free parameters in the fit. All parameters were defined at the reference epoch 2458745.0 ($\rm BJD_{TDB}$) and integrated over a baseline of 1910 d, corresponding to the full time span covered by the available photometric and RV observations.

We initially ran TRADES with PYDE, using 120 walkers for 100 000 steps. The resulting best-fitting solutions were then used as starting points for EMCEE, which we ran for 400 000 steps using 120 walkers and a thinning factor of 100. Following the approach of V. Nascimbeni et al. (2024), we adopted a mixed proposal distribution in EMCEE, applying the differential evolution proposal for 80 per cent of the walkers (B. Nelson, E. B. Ford & M. J. Payne 2014) and the snooker differential evolution proposal for the remaining 20 per cent (C. J. F. Braak & J. A. Vrugt 2008). For each of the four analyses, we chose the steps to discard as burn-in through multiple diagnostics, including the Geweke statistic (J. F. Geweke 1991), the Gelman–Rubin test (A. Gelman & D. B. Rubin 1992), the autocorrelation function (J. Goodman & J. Weare 2010), and visual inspection of the chains.

Parameter uncertainties were derived from the marginalized posterior distributions as the 68.27 per cent highest density intervals (HDIs), corresponding to the regions with the highest posterior probability. We defined the best-fitting values as the maximum a posteriori (MAP) estimates, constrained to lie within the HDIs, representing the most probable set of parameters given the data and priors.

The best-fitting parameters derived from each model, along with their corresponding priors, are reported in Table 2. The observed-minus-calculated (O − C) diagrams for all four tested configurations are shown in Figs A8–A11. Among the scenarios tested, only the third configuration, which includes a third planet located between the orbits of TOI-1422 b and c, yields planetary masses and eccentricities for both b and c that are consistent with those derived from the global fit (see Table 1). In this configuration, the additional planet d follows an eccentric orbit located near a 3:2 MMR with TOI-1422 c and a 5:3 MMR with the inner planet TOI-1422 b, suggesting that the system may be close to a 2:3:5 resonant chain. Its inferred mass is low ($M_d = 2.89^{+0.95}_{-0.82}$ $M_\oplus$; $K_d = 0.57 \pm 0.20$ m s^{-1}), suggesting that it could have remained undetected in the RV data set (see Section 3.6). The other configurations require high eccentricities and very low masses that are incompatible with the global fit constraints.

We repeated the analyses described in Section 3.2 to search for evidence of an additional transiting planet between the orbits of TOI-1422 b and TOI-1422 c, but found no significant indication. Additional transit observations of planets b and c are therefore critical to confirm and expand the TTV baseline, enabling a more robust detection and characterization of the potential perturbing companion.

3.6 Detection limits

We applied the Algorithm for the Refinement of DEtection limits via N-body stability Threshold (ARDENT; M. Stalport et al.

[3] https://github.com/lucaborsato/trades

[4] $\lambda = \mathcal{M} + \omega + \Omega$, where $\mathcal{M}$ is the mean anomaly, ω is the argument of periastron (or pericentre), and Ω is the longitude of the ascending node.

Table 2. Derived parameters of the TOI-1422 system from the four dynamical scenarios tested.

Configurations	Two planets		Three planets (inner)		Three planets (middle)		Three planets (outer)	
Parameter	Prior	MAP (HDI $\pm 1\sigma$)	Prior	MAP (HDI $\pm 1\sigma$)	Prior	MAP (HDI $\pm 1\sigma$)	Prior	MAP (HDI $\pm 1\sigma$)
TOI-1422 b								
Orbital period (P) [d]	$\mathcal{U}(12.5, 13.5)$	$12.9937^{+0.0022}_{-0.0014}$	$\mathcal{U}(12.5, 13.5)$	$12.993\,11^{+0.000\,10}_{-0.003\,10}$	$\mathcal{U}(12.5, 13.5)$	$12.9990^{+0.0011}_{-0.0026}$	$\mathcal{U}(12.5, 13.5)$	$12.992\,95^{+0.002\,78}_{-0.000\,54}$
Mass [$M_\oplus$]	$\mathcal{U}(0.1, 318)$	$0.928^{+0.807}_{-0.099}$	$\mathcal{U}(0.1, 318)$	$1.80^{+0.62}_{-0.22}$	$\mathcal{U}(0.1, 318)$	$8.58^{+2.60}_{-0.74}$	$\mathcal{U}(0.1, 318)$	$1.32^{+0.54}_{-0.44}$
Eccentricity [deg]	$\mathcal{U}(0, 0.5)$	$0.161^{+0.078}_{-0.043}$	$\mathcal{U}(0, 0.5)$	$0.048^{+0.019}_{-0.030}$	$\mathcal{U}(0, 0.5)$	$0.040^{+0.027}_{-0.035}$	$\mathcal{U}(0, 0.5)$	$0.142^{+0.095}_{-0.016}$
TOI-1422 c								
Orbital period (P) [d]	$\mathcal{U}(33, 35.5)$	$34.564\,93^{+0.001\,39}_{-0.000\,65}$	$\mathcal{U}(33, 35.5)$	$34.565\,75^{+0.002\,96}_{-0.000\,27}$	$\mathcal{U}(33, 35.5)$	$34.567\,91^{+0.002\,65}_{-0.000\,19}$	$\mathcal{U}(33, 35.5)$	$34.565\,86^{+0.000\,45}_{-0.001\,68}$
Mass [$M_\oplus$]	$\mathcal{U}(0.1, 318)$	16^{+4}_{-2}	$\mathcal{U}(0.1, 318)$	19^{+2}_{-4}	$\mathcal{U}(0.1, 318)$	14^{+2}_{-3}	$\mathcal{U}(0.1, 318)$	20^{+2}_{-4}
Eccentricity [deg]	$\mathcal{U}(0, 0.5)$	$0.198^{+0.031}_{-0.036}$	$\mathcal{U}(0, 0.5)$	$0.245^{+0.042}_{-0.013}$	$\mathcal{U}(0, 0.5)$	$0.016^{+0.029}_{-0.016}$	$\mathcal{U}(0, 0.5)$	$0.191^{+0.030}_{-0.033}$
TOI-1422 d								
Orbital period (P) [d]			$\mathcal{U}(1, 11)$	$2.189^{+4.223}_{-0.043}$	$\mathcal{U}(14, 31)$	$21.704^{+0.016}_{-0.012}$	$\mathcal{U}(40, 400)$	365^{+35}_{-25}
Mass [$M_\oplus$]			$\mathcal{U}(0.1, 318)$	$0.63^{+1.34}_{-0.54}$	$\mathcal{U}(0.1, 318)$	$2.89^{+0.95}_{-0.82}$	$\mathcal{U}(0.1, 318)$	40^{+8}_{-25}
Eccentricity [deg]			$\mathcal{U}(0, 0.5)$	$0.12^{+0.19}_{-0.12}$	$\mathcal{U}(0, 0.5)$	$0.1589^{+0.0818}_{-0.0082}$	$\mathcal{U}(0, 0.5)$	$0.414^{+0.086}_{-0.155}$
Inclination [deg]			$\mathcal{U}(80, 100)$	89^{+7}_{-6}	$\mathcal{U}(80, 100)$	91^{+6}_{-6}	$\mathcal{U}(80, 100)$	94^{+1}_{-12}

2025)[5] to compute the dynamical HARPS-N RV detection limits for the TOI-1422 system. Namely, ARDENT incorporates orbital stability constraints in addition to the data-driven limits, ensuring that only dynamically viable unseen candidates are retained.

In particular, we performed planet injection–recovery tests in the P–K parameter space by sampling 5000 points across the grid. The period of the synthetic planets was drawn from a log-uniform distribution between 2 and 100 d, the RV semi-amplitude K was drawn uniformly around the root-mean-square of the RV uncertainties, the eccentricity was sampled from the beta distribution (following D. M. Kipping 2013), and the argument of periastron ω was sampled uniformly between $-\pi$ and π, while the inclination was fixed to 90 deg. For each P–K point, we carried out 10 injection–recovery tests with different injected planets' orbital phases evenly spaced in $[-\pi; \pi]$. We applied a technique similar to A. S. Bonomo et al. (2023) for each test, where RVs at each observed timestamp are drawn from a normal distribution with the mean given by the predicted injected planet signal and the standard deviation given by the measurement uncertainty. The synthetic planet is considered recovered if the most significant signal in the periodogram is within 5 per cent of the injected period and its FAP is below 1 per cent. The detection rate of each planet in the P–K space is given by the number of detections out of the 10 tests. These experiments enable the computation of detection limits based on the RV data, namely the data-driven detection limits. In Fig. 5, we present the 95 per cent detection limits after converting K into minimal mass (brown curve).

As a second step, we investigated the dynamical viability of injected planets considering their gravitational interaction with the known ones. The motivation is that real planets must be dynamically viable in a relatively old system such as TOI-1422, the system being unstable otherwise. This additional information, which is based on orbital stability, allows us to push further the detection limits by removing unstable regions of the period–mass space (cf. M. Stalport et al. 2025, for further details). ARDENT computes the updated, dynamical detection limits from the data-driven detection limits and

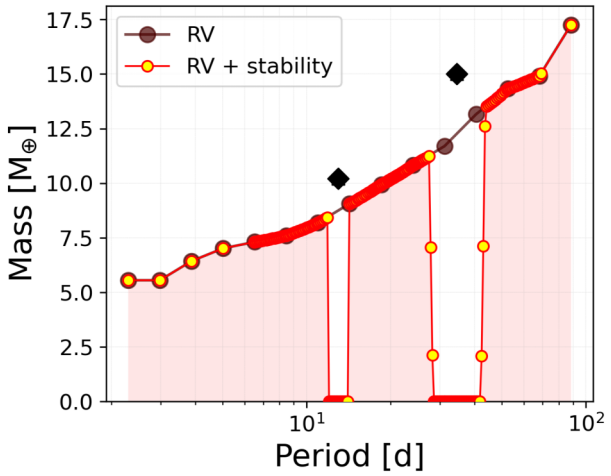

Figure 5. RV detection limits in the TOI-1422 system computed with ARDENT. The data-driven detection limits are presented in brown. The dynamical detection limits are illustrated in red–yellow. The known planets TOI-1422 b and c are indicated with the black diamond symbols. The red shaded area depicts the region of the period–mass space where additional candidates could be expected.

the orbital parameters of the two known planets (fixing here the non-significant orbital eccentricities to zero). We applied a dense period sampling around the known planets by interpolating the data-driven limit curve in 100 period bins inside the intervals $[P_i/2; 2P_i]$ (where i denoted the known planet index). The orbital stability was estimated for each point on this limit curve, and for lower masses if the former was unstable. Fig. 5 shows the outcome, with the dynamical detection limits in red.

We found significant room left for an additional third planet candidate in the system. In particular, the instability zones where no planet can exist roughly cover the ranges [11.5−14.5] and [28.6−42.3] d. Outside these period windows around the known planets, an additional candidate could exist and remain undetected with the current RV data at hand, especially if $M_p \lesssim 5\ M_\oplus$ (such as the candidate suggested in Section 3.5).

[5] https://github.com/manustalport/ardent

Table 3. Inference results for the internal compositions of TOI-1422 c. Stated errors represent 84th and 16th percentiles.

Parameters	TOI-1422 c	TOI-1422 b
$M_{\rm atm}$ ($M_\oplus$)	$0.10^{+0.03}_{-0.01}$	$1.49^{+1.15}_{-0.69}$
$M_{\rm core+mantle}$ ($M_\oplus$)	$13.90^{+2.61}_{-2.75}$	$8.43^{+1.99}_{-1.67}$
$Z_{\rm env}$	$0.37^{+0.35}_{-0.25}$	$0.24^{+0.21}_{-0.16}$

4 COMPOSITIONS

We analyse the potential composition of TOI-1422 c using a static inference model based on C. Dorn et al. (2017) with updates described in H. Luo, C. Dorn & J. Deng (2024). The model consists of three layers: an iron core, a silicate mantle, and an H_2–He–H_2O atmosphere. We assume an adiabatic temperature profile for the core and mantle and allow for both liquid and solid phases in the two layers. For liquid iron and iron alloys, we use the equation of state (EOS) by H. Luo et al. (2024). For solid iron, we use the EOS for hexagonal close packed iron (K. Hakim et al. 2018; F. Miozzi et al. 2020). For pressures below ≈125 GPa, the solid mantle mineralogy is modelled using the thermodynamical model PERPLE_X (J. A. D. Connolly 2009) considering the system of MgO, SiO_2, and FeO. At higher pressures, we define the stable minerals a priori and use their respective EOS from various sources (R. J. Hemley et al. 1992; R. A. Fischer et al. 2011; S. Faik, A. Tauschwitz & I. Iosilevskiy 2018; Y. Luo et al. 2023). The liquid mantle is modelled as a mixture of Mg_2SiO_4, SiO_2, and FeO (H. J. Melosh 2007; S. Faik et al. 2018; H. Ichikawa & T. Tsuchiya 2020; S. T. Stewart et al. 2020), and mixed using the additive volume law.

The H_2–He–H_2O atmosphere layer is modelled using the analytical description of T. Guillot (2010) and consists of an irradiated layer on top of a non-irradiated layer in radiative–convective equilibrium. The water mass fraction is given by the metallicity Z and the hydrogen–helium ratio is set to solar. The two components of the atmosphere, H_2/He and H_2O, are again mixed following the additive volume law and using the EOS by D. Saumon, G. Chabrier & H. M. van Horn (1995) for H_2/He and the ANEOS (ANalytic Equations Of State; S. Thompson 1990) for H_2O. For each model realization, the planet intrinsic luminosity is calculated following C. Mordasini (2020) and is a function of planet mass, atmospheric mass fraction, and age, for which we use the estimate of $5.1^{+3.9}_{-3.1}$ Gyr from L. Naponiello et al. (2022).

For the inference, we use a surrogate model using Polynomial Chaos Kriging (S. Marelli & B. Sudret 2014; R. Schobi, B. Sudret & J. Wiart 2015). In this approach, the global behaviour of the full physical forward model is replaced by the surrogate model leading to a strong decrease in computational cost.For our inference, the surrogate model provides high-quality fits with R-squared values (coefficient of determination) of 0.9999 and 0.9998 for planetary mass and radius, respectively. Also, rms errors are well below observational uncertainties of 0.003 and 0.01 for planetary mass and radius, respectively. Those errors of the model uncertainty are accounted for in the likelihood function. The prior parameter distribution is listed in Table B2 and the results of the inference model are summarized in Table 3 and plotted in Fig. A7. In order to explain the observed radius of TOI-1422 c, a significant atmospheric mass fraction is needed. With the assumption of an Earth-like core–mantle ratio of 0.325:0.675, we find an atmospheric mass of $M_{\rm atm} = 0.1^{+0.03}_{-0.01}$ $M_\oplus$, and a poorly constrained metallicity of $Z = 0.37^{+0.35}_{-0.25}$. We repeat the composition analysis for TOI-1422 b and find that planet b likely possesses a larger atmosphere with a lower metallicity than planet c, which directly stems from its lower density.

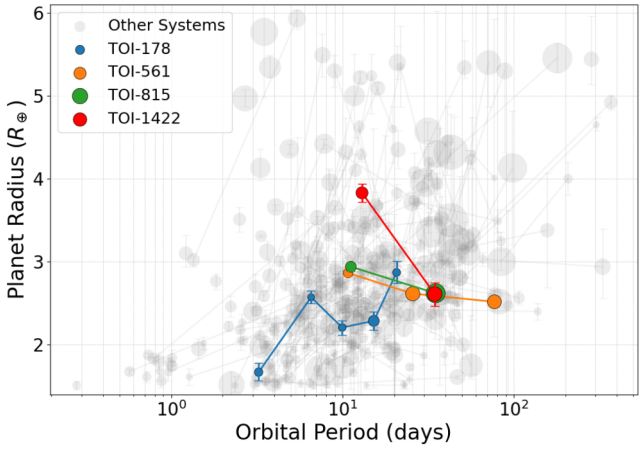

Figure 6. Multiplanet systems with at least two planets of radii 1.5 $R_\oplus$ < R_p < 6 $R_\oplus$, as taken from the NASA Exoplanet Database (J. L. Christiansen et al. 2025). The systems for which there is at least one outer planet that is both more massive and smaller than the inner planet (with significance ≥1σ) are coloured and labelled.

5 DISCUSSION

The most remarkable feature of the TOI-1422 system is its anti-ordered configuration (L. Mishra et al. 2023), defined by the relative properties of its two known planets. Although the current mass uncertainties make the two planets compatible within 1.25σ, their nominal values suggest an inversion of the commonly observed mass–radius ordering. In contrast to the widely observed trend in multiplanet systems, where planet mass and radius tend to decrease with orbital period (or at least density remains constant or decreases; L. M. Weiss & G. W. Marcy 2014), this system exhibits the opposite pattern: the outer planet, TOI-1422 c ($P_c > P_b$), is more massive ($M_c > M_b$) yet smaller than the inner planet ($R_c < R_b$), TOI-1422 b. Such anti-ordered or 'mass/density-inverted' architectures are rarely observed, despite some population synthesis models predicting a frequency of $\lesssim$8 per cent (L. Mishra et al. 2023). This discrepancy suggests that additional processes beyond simple *in situ* core accretion must have influenced the formation and evolution of this system.

To place our findings in a broader context, we searched the NASA Exoplanet Archive for confirmed multiplanet systems where at least one outer planet is both more massive and smaller than an inner planet (with differences significant at >1σ) within the radius range of 1.5–6 $R_\oplus$, corresponding to super-Earths, sub-Neptunes, and Neptune-type planets. We found only three comparable systems: TOI-178 (A. Leleu et al. 2021), TOI-561 (G. Lacedelli et al. 2021, 2022; G. Piotto et al. 2024), and TOI-815 (A. Psaridi et al. 2024). However, in these cases the anti-ordering involves only sub-Neptunes (refer to Fig. 6), whereas in TOI-1422 the inner planet is Neptune-sized.

The observed density contrast between TOI-1422 b and TOI-1422 c may point to divergent evolutionary pathways. One possibility involves late-stage giant impacts: a catastrophic collision on planet c could have stripped its primordial envelope, leaving behind a denser, core-dominated remnant (N. K. Inamdar & H. E. Schlichting 2015; S.-F. Liu et al. 2015). Alternatively, formation location and migration history may have played key roles (A. Izidoro et al. 2015;

B. Bitsch et al. 2019). Planet c could have formed in a disc region with an enhanced solid-to-gas ratio or followed a migration path that restricted its access to the natal gas reservoir, resulting in a higher CMF (Core Mass Fraction).

Moreover, it has recently been proposed that sub-Neptunes in resonant chains tend to be less dense (A. Leleu et al. 2024), although this trend may arise from biases between RV and TTV analyses. Depending on the location of the third planet responsible for the TTVs observed on planet b, this system could serve as a valuable test case for exploring that hypothesis. At present, since TOI-1422 c is not in a known resonance with any other planet, its high density is consistent with the idea that sub-Neptunes outside resonant configurations tend to be denser than those within resonant chains.

6 CONCLUSIONS

Thanks to two new *TESS* sectors (57 and 84), an expanded RV data set, and new RV reduction and analysis, we have confirmed the planet candidate TOI-1422 c. This planet orbits with a period longer than previously suggested ($P_{\rm orb} = 34.563$ d instead of $\sim$29 d) and, despite being a sub-Neptune, it is more massive than the Neptune-sized sibling TOI-1422 b ($M_{\rm c} = 14 \pm 3$ M$_\oplus$ versus $M_{\rm b} = 9.5^{+2.0}_{-1.9}$ M$_\oplus$), making TOI-1422 a rare anti-ordered system. The two mass estimates are consistent within 1.25σ, yet the comparison highlights that TOI-1422 c is significantly denser than TOI-1422 b ($\rho_{\rm c} = 4.3^{+1.3}_{-1.0}$ versus $\rho_{\rm b} = 0.93^{+0.21}_{-0.20}$). In addition, our analysis of TOI-1422 b transit times revealed significant TTVs. Such variations are not caused by gravitational perturbations from TOI-1422 c. Instead, they suggest the presence of an unseen planetary companion that may even be orbiting between them ($P_{\rm d} \approx 21$ d). The confirmation of this possibly low-mass sibling candidate ($M_{\rm d} \lesssim 4$ M$_\oplus$) will require additional photometric observations and extreme-precision ($\lesssim$1 m s^{-1}) RV measurements.

The large density contrast between the inner Neptune and the outer sub-Neptune could point to different formation or evolutionary pathways. A violent history (e.g. giant impacts or strong dynamical instabilities) might provide a possible explanation, whereas a configuration close to a three-planet MMR would instead favour a more quiescent dynamical evolution. Atmospheric characterization could help discriminate between these scenarios: a supersolar enrichment in TOI-1422 c could indicate formation beyond the ice line followed by inward migration, although alternative explanations, such as envelope enrichment through collisions or accretion of metal-rich material, cannot be excluded.

ACKNOWLEDGEMENTS

The work is based on observations made with the Italian Telescopio Nazionale Galileo (TNG) operated on the island of La Palma by the Fundacion Galileo Galilei of the INAF (Istituto Nazionale di Astrofisica) at the Spanish Observatorio del Roque de los Muchachos of the Instituto de Astrofisica de Canarias within the programme ID AOT48TAC_48. This work includes data collected with the *TESS* (Transiting Exoplanet Survey Satellite) mission, obtained from the MAST data archive at the Space Telescope Science Institute (STScI). Funding for the *TESS* mission is provided by the NASA Explorer Program. STScI is operated by the Association of Universities for Research in Astronomy, Inc., under the NASA contract NAS 5–26555. The authors acknowledge the use of public *TESS* data from pipelines at the *TESS* Science Office and at the *TESS* SPOC. Resources supporting this work were provided by the NASA High-End Computing (HEC) Program through the NASA Advanced Supercomputing (NAS) Division at Ames Research Center for the production of the SPOC data products. This research has used the Exoplanet Follow-up Observation Program (ExoFOP; DOI: 10.26134/ExoFOP5) website, which is operated by the California Institute of Technology, under contract with the National Aeronautics and Space Administration under the Exoplanet Exploration Program. This research has used the NASA Exoplanet Archive, which is operated by the California Institute of Technology, under contract with the National Aeronautics and Space Administration under the Exoplanet Exploration Program. LN acknowledges financial contribution from the INAF Large Grant 2023 'EXODEMO'. LM acknowledges the financial contribution from the PRIN (Progetti di Rilevante Interesse Nazionale) MUR (Ministero dell'Università e della Ricerca) 2022 project 2022J4H55R. PL acknowledges that this publication was produced while attending the PhD program in Space Science and Technology at the University of Trento, Cycle XXXVIII, with the support of a scholarship co-financed by the Ministerial Decree no. 351 of 2022 April 9, based on the NRRP – funded by the European Union – NextGenerationEU – Mission 4 'Education and Research', Component 2 'From Research to Business', Investment 3.3 – CUP E63C22001340001. MS thanks the Belgian Federal Science Policy Office (BELSPO) for the provision of financial support in the framework of the PRODEX Programme of the ESA under contract number C4000140754. CD acknowledges support from the Swiss National Science Foundation under grant TMSGI2_211313. Parts of this work have been carried out within the framework of the NCCR PlanetS supported by the Swiss National Science Foundation under grants 51NF40_182901 and 51NF40_205606. The authors acknowledge the support of the INAF Guest Observer Grant (Normal) 'ArMS: the Ariel Masses Survey Large Program at the TNG', according to the INAF Fundamental Astrophysics funding scheme.

DATA AVAILABILITY

The photometric data used in this manuscript are available on the MAST, while the entire RV data set has been included in Table B1.

REFERENCES

Agol E., Steffen J., Sari R., Clarkson W., 2005, MNRAS, 359, 567
Bitsch B., Izidoro A., Johansen A., Raymond S. N., Morbidelli A., Lambrechts M., Jacobson S. A., 2019, A&A, 623, A88
Blunt S. et al., 2023, AJ, 166, 62
Bonomo A. S. et al., 2019, Nat. Astron., 3, 416
Bonomo A. S. et al., 2023, A&A, 677, A33
Borsato L. et al., 2019, MNRAS, 484, 3233
Borsato L. et al., 2021, MNRAS, 506, 3810
Borsato L. et al., 2024, A&A, 689, A52
Borsato L., Marzari F., Nascimbeni V., Piotto G., Granata V., Bedin L. R., Malavolta L., 2014, A&A, 571, A38
Chatterjee S., Tan J. C., 2014, ApJ, 780, 53
Chen J., Kipping D., 2017, ApJ, 834, 17
Christiansen J. L. et al., 2025, Planet. Sci. J., 6, 186
Claret A., 2017, A&A, 600, A30
Connolly J. A. D., 2009, in Geochemistry, Geophysics, Geosystems, Vol. 10, Issue 10, The Geodynamic Equation of State: What and How. Hoboken, New Jersey
Cosentino R. et al., 2012, in Proc. SPIE Conf. Ser. Vol. 8446, Ground-based and Airborne Instrumentation for Astronomy IV. SPIE, Bellingham, p. 84461V

Dorn C., Venturini J., Khan A., Heng K., Alibert Y., Helled R., Rivoldini A., Benz W., 2017, A&A, 597, A37
Dumusque X. et al., 2021, A&A, 648, A103
Eastman J., Gaudi B. S., Agol E., 2013, PASP, 125, 83
Espinoza N., 2018, Res. Notes Am. Astron. Soc., 2, 209
Espinoza N., Kossakowski D., Brahm R., 2019, MNRAS, 490, 2262
Faik S., Tauschwitz A., Iosilevskiy I., 2018, Comput. Phys. Commun., 227, 117
Fischer R. A., Campbell A. J., Shofner G. A., Lord O. T., Dera P., Prakapenka V. B., 2011, Earth Planet. Sci. Lett., 304, 496
Fortney J. J., Marley M. S., Barnes J. W., 2007, ApJ, 659, 1661
Gelman A., Rubin D. B., 1992, Stat. Sci., 7, 457
Geweke J. F., 1991, Staff Report 148, Evaluating the Accuracy of Sampling-based Approaches to the Calculation of Posterior Moments. Federal Reserve Bank of Minneapolis, Minneapolis, Minnesota
Goodman J., Weare J., 2010, Commun. Appl. Math. Comput. Sci., 5, 65
Guillot T., 2010, A&A, 520, A27
Hakim K., Rivoldini A., Van Hoolst T., Cottenier S., Jaeken J., Chust T., Steinle-Neumann G., 2018, Icarus, 313, 61
Hemley R. J., Stixrude L., Fei Y., Mao H. K., 1992, in High-Pressure Research: Application to Earth and Planetary Sciences. American Geophysical Union (AGU), Washington, D.C., United States, p. 183
Hippke M., Heller R., 2019, A&A, 623, A39
Holman M. J., Murray N. W., 2005, Science, 307, 1288
Howe A. R., Becker J. C., Stark C. C., Adams F. C., 2025, AJ, 169, 149
Ichikawa H., Tsuchiya T., 2020, Minerals, 10, 59
Inamdar N. K., Schlichting H. E., 2015, MNRAS, 448, 1751
Izidoro A., Raymond S. N., Morbidelli A., Hersant F., Pierens A., 2015, ApJ, 800, L22
Jenkins J. M. et al., 2016, in Chiozzi G., Guzman J. C., eds, Proc. SPIE Conf. Ser. Vol. 9913, Software and Cyberinfrastructure for Astronomy IV. SPIE, Bellingham, p. 99133E
Kipping D. M., 2013, MNRAS, 434, L51
Korth J. et al., 2024, ApJ, 971, L28
Kovács G., Zucker S., Mazeh T., 2002, A&A, 391, 369
Lacedelli G. et al., 2021, MNRAS, 501, 4148
Lacedelli G. et al., 2022, MNRAS, 511, 4551
Leleu A. et al., 2021, A&A, 649, A26
Leleu A. et al., 2024, A&A, 687, L1
Leonardi P. et al., 2024, A&A, 686, A84
Liu S.-F., Hori Y., Lin D. N. C., Asphaug E., 2015, ApJ, 812, 164
Lopez E. D., Fortney J. J., 2014, ApJ, 792, 1
Luo H., Dorn C., Deng J., 2024, Nat. Astron., 8, 1399
Luo Y., Xiang S., Li J., Wu J., Liu L., Li J., Xian Y., Wu R., 2023, Phys. Rev. B, 107, 134116
Malavolta L. et al., 2017, AJ, 153, 224
Marelli S., Sudret B., 2014, in 2nd Int. Conf. on Vulnerability, Risk Analysis and Management, Vulnerability, Uncertainty, and Risk: Quantification, Mitigation, and Management. Reston, Virginia, USA, p. 2554
Melosh H. J., 2007, Meteorit. Planet. Sci., 42, 2079
Millholland S., Wang S., Laughlin G., 2017, ApJ, 849, L33
Miozzi F., Matas J., Guignot N., Badro J., Siebert J., Fiquet G., 2020, Minerals, 10, 100
Mishra L., Alibert Y., Udry S., Mordasini C., 2023, A&A, 670, A68
Mordasini C., 2020, A&A, 638, A52
Naponiello L. et al., 2022, A&A, 667, A8
Nascimbeni V. et al., 2023, A&A, 673, A42
Nascimbeni V. et al., 2024, A&A, 690, A349
Nelson B., Ford E. B., Payne M. J., 2014, ApJS, 210, 11
Nespral D. et al., 2017, A&A, 601, A128
Patra K. C., Winn J. N., Holman M. J., Yu L., Deming D., Dai F., 2017, AJ, 154, 4
Petigura E. A. et al., 2018, AJ, 156, 89
Piotto G. et al., 2024, MNRAS, 535, 2763
Polanski A. S. et al., 2024, ApJS, 272, 32
Psaridi A. et al., 2024, A&A, 685, A5
Ragozzine D., Wolf A. S., 2009, ApJ, 698, 1778
Rajpaul V., Aigrain S., Osborne M. A., Reece S., Roberts S., 2015, MNRAS, 452, 2269
Rasio F. A., Tout C. A., Lubow S. H., Livio M., 1996, ApJ, 470, 1187
Saumon D., Chabrier G., van Horn H. M., 1995, ApJS, 99, 713
Schobi R., Sudret B., Wiart J., 2015, Int. J. Uncertain. Quantif., 5 171
Smith J. C. et al., 2012, PASP, 124, 1000
Smith L. C. et al., 2025, MNRAS, 539, 297
Stalport M., Cretignier M., Naponiello L., Van Grootel V., 2025, A&A, 702, L2
Stewart S. T. et al., 2020, in AIP Conf. Proc. Vol. 2272, The Shock Physics of Giant Impacts: Key Requirements for the Equations of State. Am. Inst. Phys., New York, p. 080003
Stumpe M. C. et al., 2012, PASP, 124, 985
Stumpe M. C., Smith J. C., Catanzarite J. H., Van Cleve J. E., Jenkins J. M., Twicken J. D., Girouard F. R., 2014, PASP, 126, 100
ter Braak C. J. F., Vrugt J. A., 2008, Stat. Comput., 18, 435
Thompson S., 1990, Lab. Doc. SAND89-2951. Sandia National Laboratories, Albuquerque, New Mexico
Tinetti G. et al., 2018, Exp. Astron., 46, 135
Vogt S. S. et al., 1994, in Crawford D. L., Craine E. R., eds, Proc. SPIE Conf. Ser. Vol. 2198, Instrumentation in Astronomy VIII. SPIE, Bellingham, p. 362
Weiss L. M. et al., 2018, AJ, 155, 48
Weiss L. M., Marcy G. W., 2014, ApJ, 783, L6
Winn J. N., 2010, in Seager S., ed., Exoplanets. University of Arizona Press, Tucson, AZ, p. 55
Winn J. N., Fabrycky D. C., 2015, ARA&A, 53, 409

APPENDIX A: ADDITIONAL FIGURES

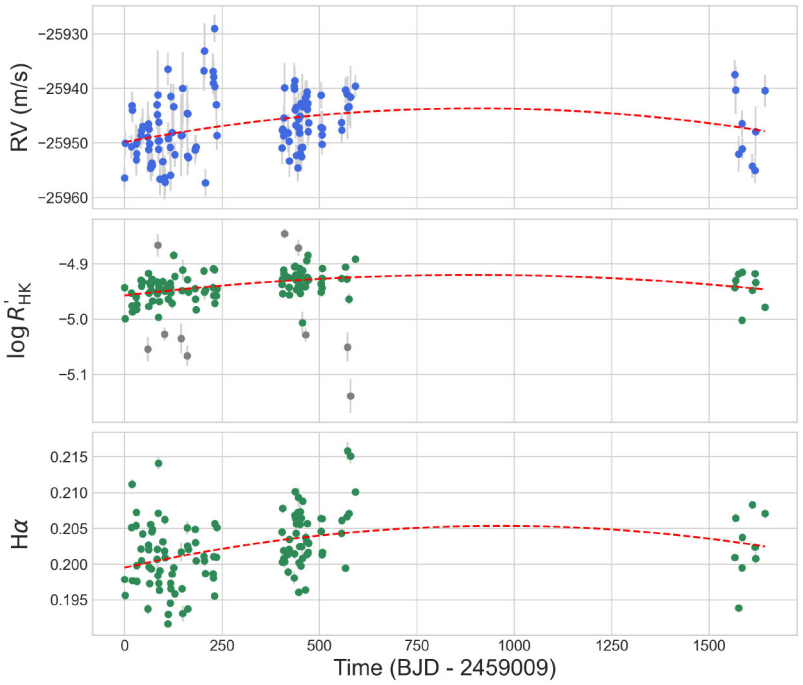

Figure A1. RV time series along with those of the chromospheric index log R'_{HK}, the H α line, and the Na I line. The dashed line shows a simple quadratic fit to each data set, while the grey circles are points that deviate more than 3σ from the median and have not been considered for the fit.

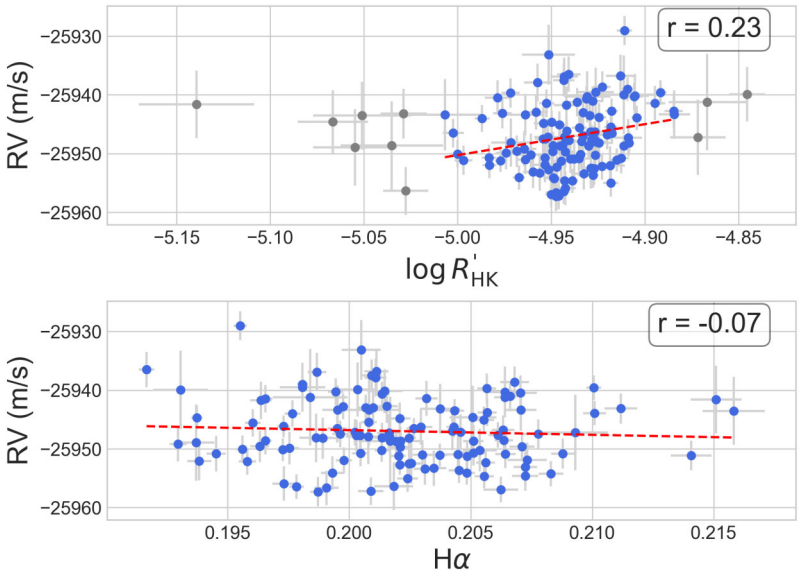

Figure A2. Correlation between RVs and stellar activity indicators. The dashed line represents the best linear fit to the data, and the corresponding Pearson correlation coefficient (r) is reported in the top-right corner of each panel. The grey circles are points that deviate more than 3σ from the median and have not been considered.

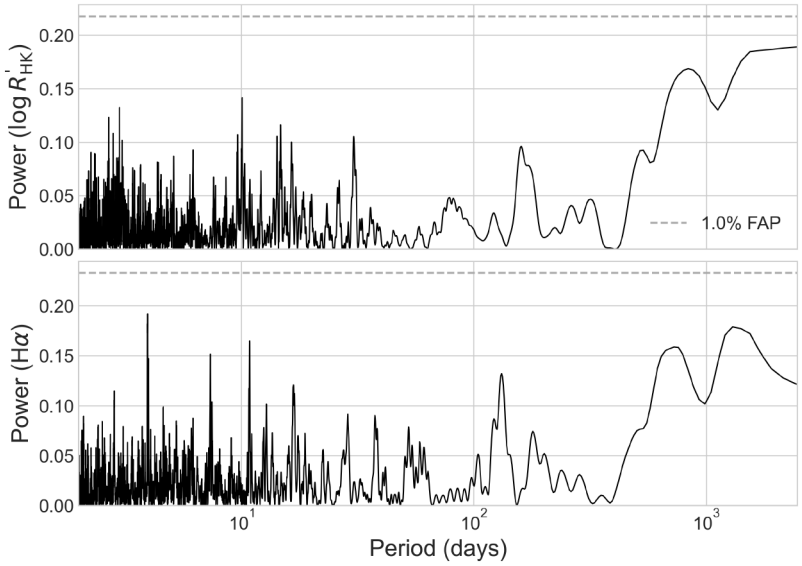

Figure A3. GLS periodograms of the log R'_{HK} and Hα indices. No strong activity peak is revealed; however, both show tentative long-period signals.

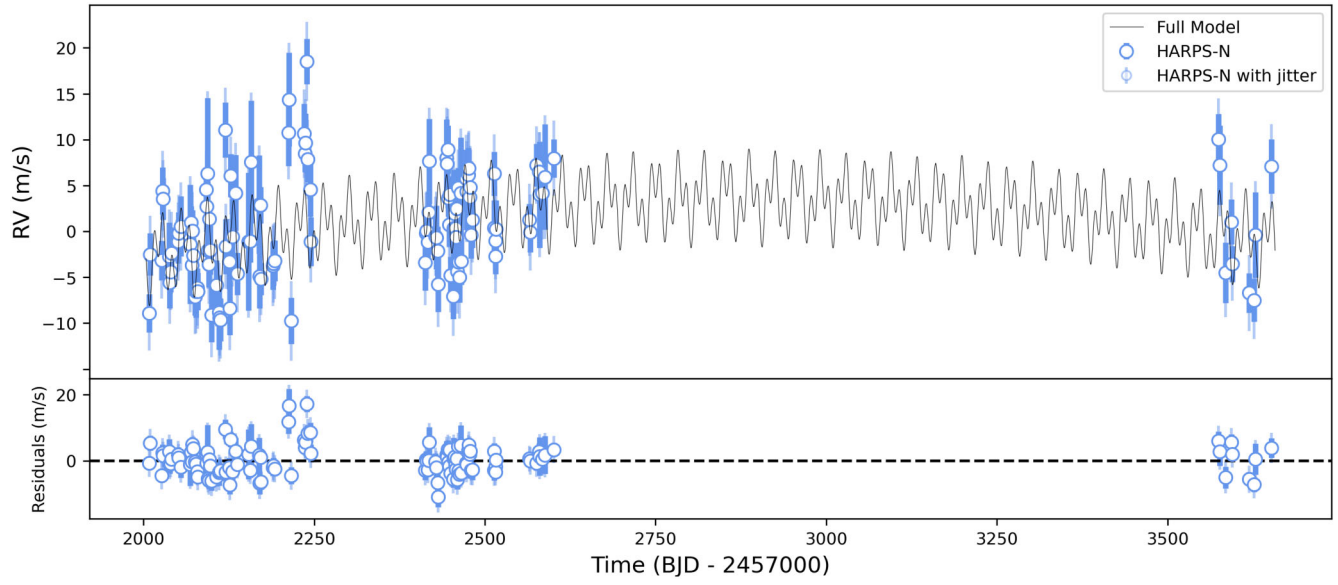

Figure A4. The HARPS-N RV data set of TOI-1422, along with the global model derived in this paper (top panel) and its residuals (bottom panel).

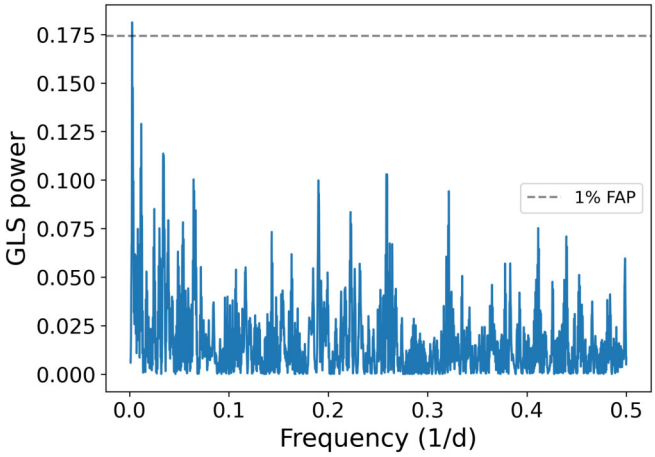

Figure A5. GLS periodogram of the RV residuals from the adopted model. The horizontal dashed line marks the 1 per cent FAP.

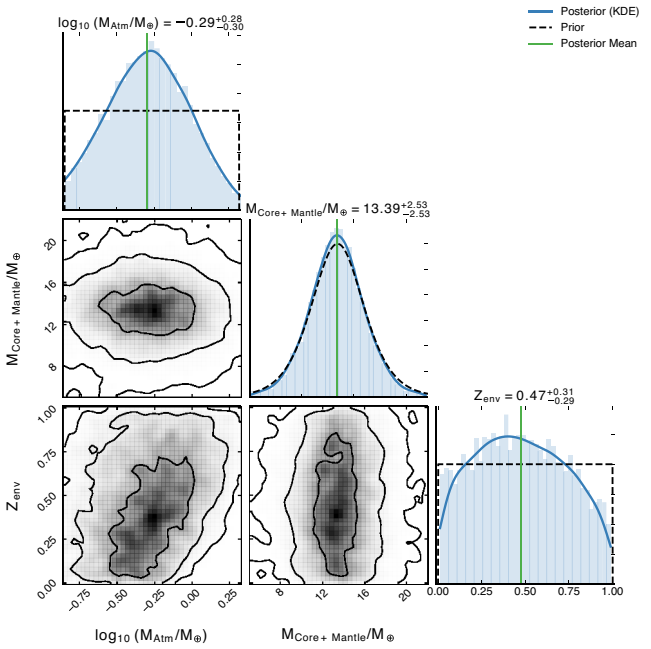

Figure A7. 1D and 2D posterior distribution of interior properties of TOI-1422 c.

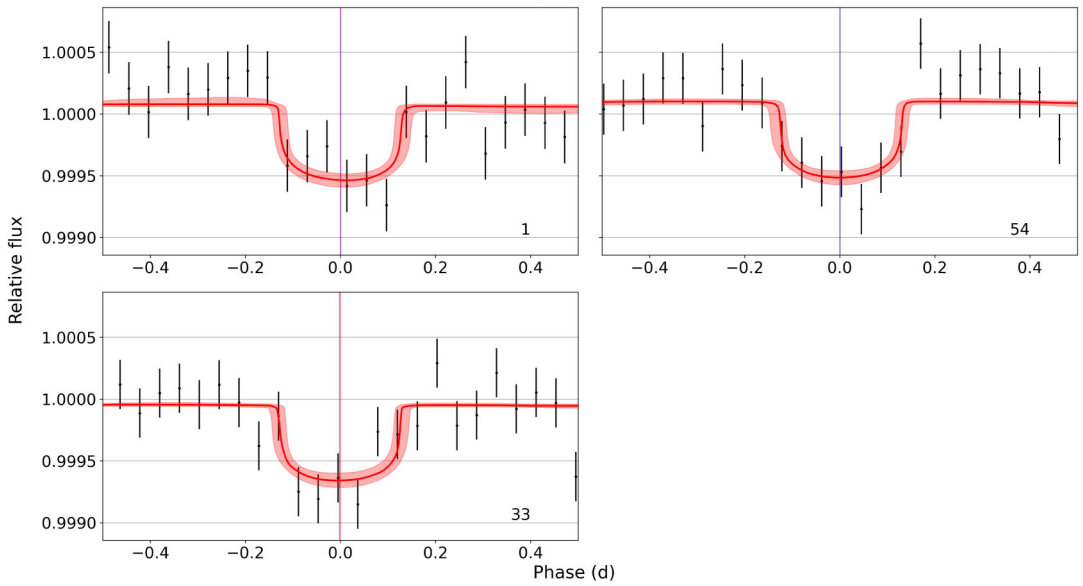

Figure A6. The three transits of TOI-1422 c fitted independently. The centre of the transits are indicated by the vertical lines.

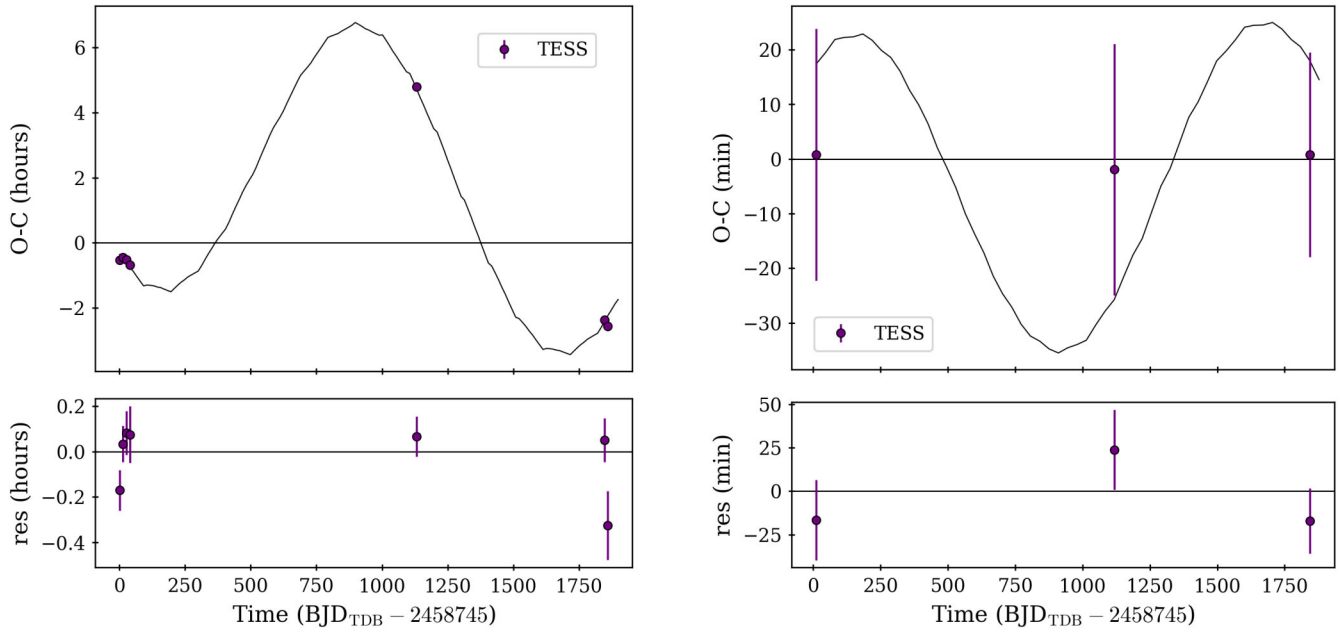

Figure A8. O − C diagrams of TOI-1422 b (left) and c (right) of configuration (1). Upper panel: The best-fitting TRADES model is shown as a black line. Lower panel: Residuals with respect to the best-fitting model.

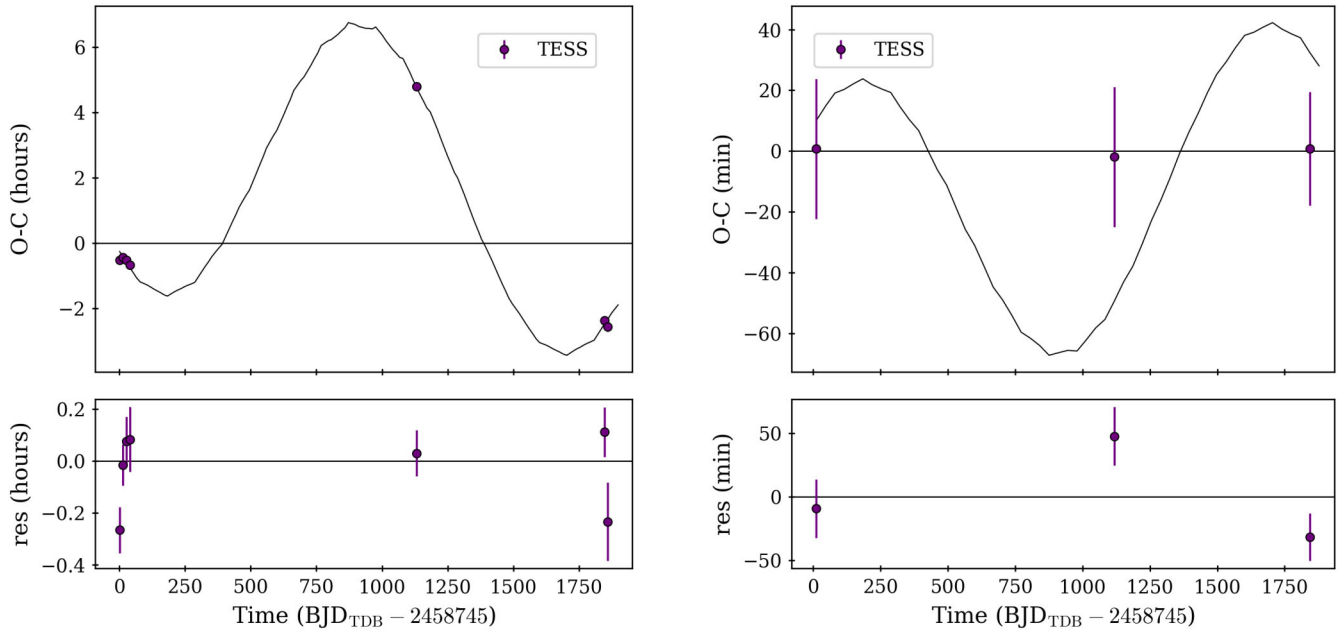

Figure A9. O − C diagrams of TOI-1422 b (left) and c (right) of configuration (2). Upper panel: The best-fitting TRADES model is shown as a black line. Lower panel: Residuals with respect to the best-fitting model.

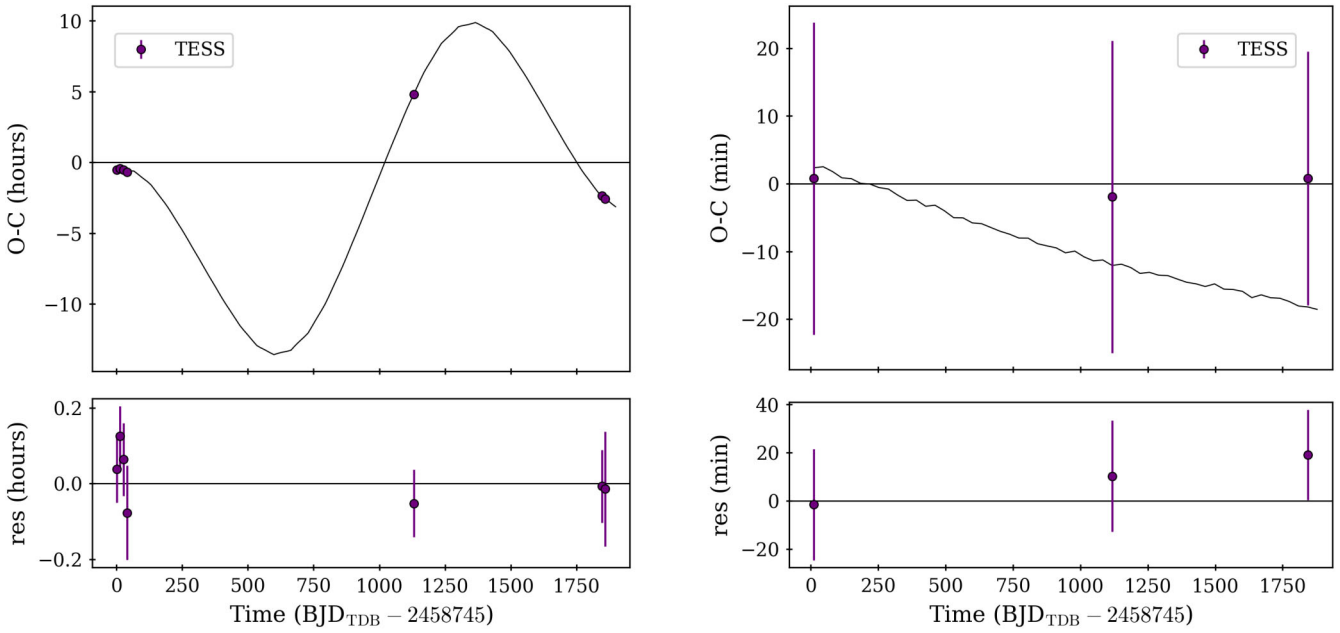

Figure A10. O − C diagrams of TOI-1422 b (left) and c (right) of configuration (3). Upper panel: The best-fitting TRADES model is shown as a black line. Lower panel: Residuals with respect to the best-fitting model.

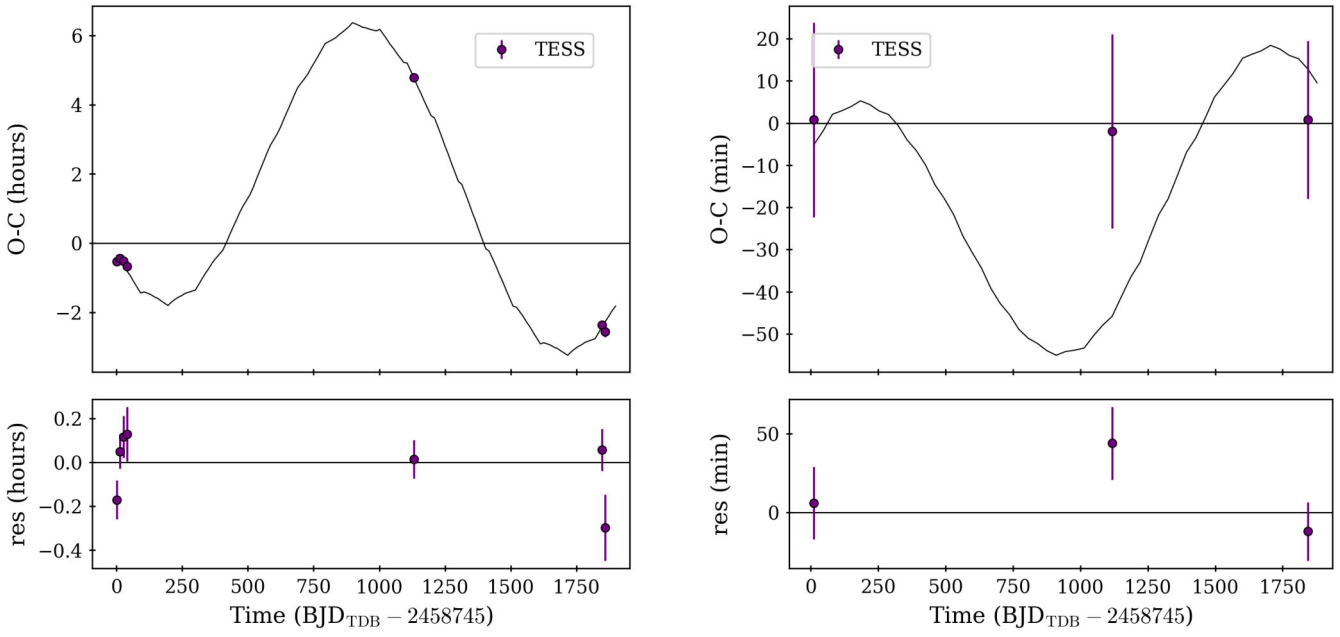

Figure A11. O − C diagrams of TOI-1422 b (left) and c (right) of configuration (4). Upper panel: The best-fitting TRADES model is shown as a black line. Lower panel: Residuals with respect to the best-fitting model.

APPENDIX B: ADDITIONAL TABLES

Table B1. HARPS-N RV data points and activity indices of TOI-1422, including the full width at half-maximum (FWHM), the contrast, and the bisector inverse span (BIS) of the cross-correlation function.

BJD_{UTC} −2457000 [d]	RV [m s^{-1}]	$\pm1\sigma_{RV}$	FWHM –	FWHM err. –	Contrast –	Cont. err. –	BIS –	BIS err. –	$I_{H\alpha}$ –	$I_{H\alpha}$ err. –	I_{Na1} –	I_{Na1} err. –	$\log R'_{HK}$ –	$\log R'_{HK}$ err. –
2008.69430381	−25 956.44	2.08	7.2146	0.0042	51.788	0.030	−0.0488	0.0042	0.197 83	0.000 30	0.335 09	0.000 21	−4.9432	0.0032
2009.71241443	−25 950.05	2.31	7.2199	0.0046	51.770	0.033	−0.0390	0.0046	0.195 60	0.000 26	0.324 84	0.000 23	−4.9999	0.0044
2026.66268375	−25 950.71	2.14	7.2119	0.0043	51.869	0.031	−0.0432	0.0043	0.205 11	0.000 45	0.342 97	0.000 25	−4.9532	0.0035
2027.72143979	−25 943.15	2.57	7.2173	0.0051	51.747	0.037	−0.0461	0.0051	0.211 18	0.000 67	0.343 33	0.000 35	−4.9760	0.0049
2028.69382541	−25 944.00	2.27	7.2223	0.0045	51.819	0.033	−0.0443	0.0045	0.197 67	0.000 33	0.330 05	0.000 23	−4.9868	0.0041
2037.71006166	−25 950.23	3.65	7.2277	0.0073	51.656	0.052	−0.0425	0.0073	0.205 37	0.000 70	0.335 09	0.000 45	−4.9608	0.0080
2038.71085062	−25 953.11	2.80	7.2140	0.0056	51.749	0.040	−0.0527	0.0056	0.207 25	0.000 49	0.335 39	0.000 32	−4.9597	0.0054
2039.71726650	−25 951.96	2.22	7.2206	0.0044	51.826	0.032	−0.0418	0.0044	0.199 78	0.000 33	0.329 30	0.000 23	−4.9829	0.0038
2040.70485007	−25 949.89	2.78	7.2161	0.0056	51.878	0.040	−0.0562	0.0056	0.197 54	0.000 39	0.327 58	0.000 30	−4.9741	0.0054
2050.69869911	−25 948.66	2.38	7.2344	0.0048	51.767	0.034	−0.0456	0.0048	0.202 11	0.000 49	0.331 44	0.000 28	−4.9300	0.0037
2051.69941908	−25 947.75	2.28	7.2149	0.0046	51.827	0.033	−0.0531	0.0046	0.200 46	0.000 32	0.326 71	0.000 24	−4.9405	0.0036
2054.72485199	−25 947.00	3.27	7.2133	0.0065	51.744	0.047	−0.0440	0.0065	0.204 25	0.000 58	0.329 31	0.000 39	−4.9329	0.0066
2068.61657773	−25 948.94	6.50	7.2087	0.0130	51.636	0.093	−0.0475	0.0130	0.193 69	0.000 76	0.312 91	0.000 78	−5.0547	0.0223
2069.66518268	−25 946.55	1.78	7.2208	0.0036	51.812	0.026	−0.0387	0.0036	0.202 66	0.000 30	0.332 76	0.000 18	−4.9176	0.0022
2070.70331840	−25 951.22	1.90	7.2178	0.0038	51.831	0.027	−0.0422	0.0038	0.202 03	0.000 30	0.332 13	0.000 19	−4.9771	0.0029
2071.70861407	−25 947.49	2.27	7.2323	0.0045	51.812	0.033	−0.0404	0.0045	0.199 63	0.000 32	0.328 95	0.000 23	−4.9530	0.0038
2072.70390704	−25 950.16	1.92	7.2210	0.0038	51.772	0.027	−0.0519	0.0038	0.197 26	0.000 23	0.327 07	0.000 18	−4.9343	0.0026
2075.64050686	−25 954.65	2.07	7.2164	0.0041	51.816	0.030	−0.0435	0.0041	0.205 55	0.000 39	0.339 96	0.000 23	−4.9387	0.0031
2076.71172723	−25 954.10	2.86	7.2234	0.0057	51.785	0.041	−0.0508	0.0057	0.199 31	0.000 49	0.330 82	0.000 32	−4.9489	0.0052
2078.68209378	−25 953.69	2.11	7.2294	0.0042	51.816	0.030	−0.0537	0.0042	0.204 51	0.000 42	0.334 92	0.000 24	−4.9276	0.0030
2079.69157744	−25 954.09	2.05	7.2230	0.0041	51.847	0.029	−0.0500	0.0041	0.204 84	0.000 33	0.334 93	0.000 21	−4.9673	0.0032
2091.68517699	−25 942.99	2.22	7.2221	0.0044	51.816	0.032	−0.0457	0.0044	0.200 67	0.000 33	0.331 32	0.000 22	−4.9330	0.0035
2092.62642253	−25 944.84	2.75	7.2247	0.0055	51.674	0.039	−0.0514	0.0055	0.202 09	0.000 43	0.331 97	0.000 30	−4.9541	0.0052
2093.65167345	−25 941.22	8.21	7.1941	0.0164	51.506	0.118	−0.0339	0.0164	0.198 40	0.001 54	0.330 55	0.001 11	−4.8667	0.0206
2094.60878996	−25 949.64	2.19	7.2241	0.0044	51.758	0.031	−0.0438	0.0044	0.207 11	0.000 52	0.340 59	0.000 26	−4.9491	0.0034
2095.61250010	−25 951.13	2.51	7.2212	0.0050	51.779	0.036	−0.0429	0.0050	0.214 08	0.000 84	0.344 27	0.000 36	−4.9968	0.0048
2096.63043591	−25 946.18	1.86	7.2069	0.0037	51.808	0.027	−0.0468	0.0037	0.197 29	0.000 25	0.329 61	0.000 18	−4.9417	0.0025
2097.66492584	−25 949.58	2.68	7.2272	0.0054	51.699	0.038	−0.0420	0.0054	0.196 31	0.000 38	0.326 78	0.000 28	−4.9684	0.0050
2099.64055626	−25 956.66	2.95	7.2259	0.0059	51.747	0.042	−0.0436	0.0059	0.199 06	0.000 50	0.331 33	0.000 34	−4.9475	0.0055
2106.65935375	−25 953.42	2.74	7.2134	0.0055	51.846	0.039	−0.0509	0.0055	0.203 12	0.000 46	0.333 64	0.000 31	−4.9325	0.0049
2110.71647151	−25 956.36	4.06	7.2267	0.0081	51.780	0.058	−0.0364	0.0081	0.201 83	0.000 80	0.334 37	0.000 50	−5.0276	0.0121
2111.55350057	−25 956.94	2.17	7.2319	0.0043	51.782	0.031	−0.0471	0.0043	0.206 24	0.000 72	0.341 76	0.000 29	−4.9499	0.0033
2112.58877718	−25 957.19	2.32	7.2189	0.0046	51.876	0.033	−0.0499	0.0046	0.200 88	0.000 53	0.338 32	0.000 28	−4.9460	0.0037
2119.69094709	−25 936.50	3.00	7.2213	0.0060	51.738	0.043	−0.0435	0.0060	0.191 66	0.000 32	0.310 36	0.000 30	−4.9406	0.0063
2120.67760594	−25 949.18	3.00	7.2300	0.0060	51.725	0.043	−0.0433	0.0060	0.192 95	0.000 36	0.318 26	0.000 31	−4.9643	0.0065
2125.54522998	−25 950.83	3.03	7.2127	0.0061	51.670	0.043	−0.0465	0.0061	0.194 53	0.000 40	0.324 82	0.000 33	−4.9352	0.0057
2126.56916834	−25 955.91	2.91	7.2154	0.0058	51.721	0.042	−0.0540	0.0058	0.197 30	0.000 47	0.326 88	0.000 33	−4.9425	0.0055
2127.63495900	−25 941.46	2.34	7.1975	0.0047	51.835	0.034	−0.0335	0.0047	0.196 55	0.000 29	0.322 74	0.000 23	−4.9525	0.0041
2130.59708730	−25 948.12	4.13	7.2245	0.0083	51.662	0.059	−0.0473	0.0083	0.198 63	0.000 69	0.327 17	0.000 49	−4.9716	0.0103
2134.62091775	−25 943.35	4.14	7.2372	0.0083	51.633	0.059	−0.0463	0.0083	0.199 51	0.000 62	0.324 05	0.000 47	−4.8843	0.0084
2137.55167183	−25 952.16	2.29	7.2271	0.0046	51.752	0.033	−0.0377	0.0046	0.195 81	0.000 36	0.330 82	0.000 24	−4.9229	0.0034
2153.56157966	−25 948.65	7.52	7.2083	0.0150	50.864	0.106	−0.0698	0.0150	0.201 68	0.001 31	0.338 42	0.000 96	−5.0351	0.0273
2156.54073685	−25 948.62	2.32	7.2215	0.0046	51.739	0.033	−0.0405	0.0046	0.196 54	0.000 27	0.326 61	0.000 22	−4.9489	0.0039
2157.58253018	−25 939.99	6.69	7.2355	0.0134	51.239	0.095	−0.0508	0.0134	0.193 06	0.001 13	0.332 33	0.000 83	−4.9111	0.0186
2169.31414581	−25 944.61	5.37	7.2447	0.0107	51.639	0.077	−0.0544	0.0107	0.205 09	0.000 97	0.357 14	0.000 70	−5.0666	0.0187
2170.34456074	−25 952.45	3.49	7.2255	0.0070	51.749	0.050	−0.0483	0.0070	0.202 55	0.000 51	0.336 12	0.000 39	−4.9288	0.0072
2171.31790533	−25 944.67	1.99	7.2305	0.0040	51.831	0.029	−0.0426	0.0040	0.193 72	0.000 23	0.328 33	0.000 18	−4.9499	0.0030
2172.31372841	−25 952.72	1.73	7.2256	0.0035	51.866	0.025	−0.0493	0.0035	0.202 07	0.000 25	0.333 23	0.000 16	−4.9514	0.0023
2189.39470134	−25 951.29	2.60	7.2318	0.0052	51.769	0.037	−0.0409	0.0052	0.204 85	0.000 39	0.334 82	0.000 28	−4.9447	0.0048
2190.35969016	−25 951.01	2.46	7.2219	0.0049	51.827	0.035	−0.0447	0.0049	0.203 02	0.000 41	0.340 96	0.000 27	−4.9638	0.0046
2192.33694562	−25 950.74	2.22	7.2349	0.0044	51.773	0.032	−0.0394	0.0044	0.200 46	0.000 35	0.338 83	0.000 24	−4.9831	0.0039
2212.37435503	−25 936.78	3.64	7.2407	0.0073	51.693	0.052	−0.0481	0.0073	0.201 12	0.000 50	0.330 53	0.000 41	−4.9130	0.0076
2213.42144850	−25 933.17	5.10	7.2441	0.0102	51.627	0.073	−0.0424	0.0102	0.200 49	0.000 81	0.340 85	0.000 63	−4.9514	0.0141
2216.40464082	−25 957.30	2.52	7.2358	0.0050	51.766	0.036	−0.0469	0.0050	0.198 72	0.000 33	0.331 91	0.000 26	−4.9473	0.0047
2235.36800056	−25 936.90	3.27	7.2153	0.0065	51.681	0.047	−0.0392	0.0065	0.198 67	0.000 39	0.321 70	0.000 34	−4.9430	0.0073
2236.31848652	−25 939.04	2.01	7.2107	0.0040	51.788	0.029	−0.0386	0.0040	0.198 08	0.000 22	0.321 28	0.000 18	−4.9093	0.0029
2237.32445636	−25 937.89	3.21	7.2161	0.0064	51.689	0.046	−0.0480	0.0064	0.201 09	0.000 45	0.335 75	0.000 35	−4.9572	0.0072
2239.31347520	−25 929.04	2.48	7.2663	0.0050	51.486	0.035	−0.0354	0.0050	0.195 51	0.000 27	0.330 26	0.000 24	−4.9109	0.0041
2240.31392795	−25 939.68	2.49	7.2404	0.0050	51.576	0.035	−0.0372	0.0050	0.205 66	0.000 39	0.344 68	0.000 26	−4.9716	0.0048
2244.31787105	−25 942.97	2.97	7.2368	0.0059	51.597	0.042	−0.0408	0.0059	0.200 98	0.000 49	0.338 65	0.000 33	−4.9580	0.0062
2245.32061706	−25 948.66	2.68	7.2440	0.0054	51.710	0.038	−0.0410	0.0054	0.205 11	0.000 42	0.336 34	0.000 29	−4.9453	0.0051
2412.68949053	−25 950.92	3.05	7.2197	0.0061	51.732	0.044	−0.0454	0.0061	0.204 47	0.000 62	0.336 86	0.000 37	−4.9377	0.0059
2413.66459085	−25 947.71	2.65	7.2183	0.0053	51.823	0.038	−0.0441	0.0053	0.200 30	0.000 40	0.328 45	0.000 28	−4.9284	0.0048
2414.68966285	−25 947.48	2.49	7.2253	0.0050	51.766	0.036	−0.0377	0.0050	0.207 77	0.000 70	0.337 67	0.000 34	−4.9543	0.0044

Table B1 – *continued*

BJD_{UTC} −2457000 [d]	RV [m s^{-1}]	$\pm1\sigma_{RV}$	FWHM –	FWHM err. –	Contrast –	Cont. err. –	BIS –	BIS err. –	$I_{H\alpha}$ –	$I_{H\alpha}$ err. –	I_{Na1} –	I_{Na1} err. –	log R'_{HK} –	log R'_{HK} err. –
2416.63195876	−25 948.72	1.84	7.2256	0.0037	51.752	0.026	−0.0450	0.0037	0.201 93	0.000 25	0.334 40	0.000 17	−4.9112	0.0024
2417.65217737	−25 945.45	2.23	7.2299	0.0045	51.679	0.032	−0.0452	0.0045	0.200 80	0.000 33	0.334 41	0.000 23	−4.9182	0.0034
2418.65567006	−25 939.90	4.63	7.2226	0.0093	51.583	0.066	−0.0491	0.0093	0.200 35	0.000 82	0.333 48	0.000 58	−4.8454	0.0094
2427.73262001	−25 948.08	2.51	7.2244	0.0050	51.677	0.036	−0.0372	0.0050	0.201 36	0.000 34	0.326 94	0.000 25	−4.9256	0.0042
2428.66099085	−25 948.20	3.48	7.2369	0.0070	51.680	0.050	−0.0446	0.0070	0.198 91	0.000 59	0.334 90	0.000 40	−4.9245	0.0073
2430.67069466	−25 949.69	2.69	7.2243	0.0054	51.826	0.039	−0.0456	0.0054	0.202 10	0.000 49	0.334 03	0.000 30	−4.9424	0.0051
2431.71441182	−25 953.31	3.01	7.2281	0.0060	51.773	0.043	−0.0573	0.0060	0.203 48	0.000 51	0.334 19	0.000 34	−4.9562	0.0063
2443.66167945	−25 939.53	4.19	7.2331	0.0084	51.677	0.060	−0.0390	0.0084	0.198 08	0.000 94	0.338 65	0.000 55	−4.9262	0.0096
2444.58062692	−25 940.18	3.73	7.2304	0.0075	51.632	0.053	−0.0418	0.0075	0.201 46	0.000 72	0.335 26	0.000 46	−4.9054	0.0077
2445.59714044	−25 938.62	2.63	7.2310	0.0053	51.704	0.038	−0.0521	0.0053	0.206 81	0.000 60	0.338 16	0.000 32	−4.9227	0.0045
2446.60954406	−25 943.91	2.04	7.2346	0.0041	51.707	0.029	−0.0401	0.0041	0.210 10	0.000 47	0.340 39	0.000 23	−4.9044	0.0028
2447.61816721	−25 946.79	2.45	7.2228	0.0049	51.731	0.035	−0.0402	0.0049	0.206 34	0.000 47	0.335 73	0.000 28	−4.9201	0.0040
2448.59247450	−25 943.51	1.99	7.2276	0.0040	51.736	0.028	−0.0471	0.0040	0.204 33	0.000 39	0.339 05	0.000 21	−4.9295	0.0028
2449.61747375	−25 952.32	2.00	7.2316	0.0040	51.709	0.029	−0.0501	0.0040	0.205 61	0.000 39	0.338 36	0.000 22	−4.9469	0.0030
2453.58219427	−25 954.60	2.51	7.2317	0.0050	51.731	0.036	−0.0508	0.0050	0.207 24	0.000 54	0.333 98	0.000 30	−4.9429	0.0044
2454.66812667	−25 947.21	6.43	7.1978	0.0129	51.332	0.092	−0.0655	0.0129	0.209 30	0.001 34	0.325 52	0.000 83	−4.8716	0.0148
2455.68216977	−25 945.60	2.35	7.2287	0.0047	51.761	0.034	−0.0504	0.0047	0.196 03	0.000 32	0.325 19	0.000 23	−4.9350	0.0040
2456.70439482	−25 947.19	2.27	7.2287	0.0045	51.760	0.032	−0.0431	0.0045	0.200 24	0.000 32	0.329 57	0.000 23	−4.9428	0.0037
2457.65525719	−25 948.19	1.99	7.2315	0.0040	51.728	0.028	−0.0453	0.0040	0.202 46	0.000 29	0.332 03	0.000 20	−4.9084	0.0027
2458.62496853	−25 945.07	2.27	7.2291	0.0045	51.777	0.033	−0.0417	0.0045	0.205 54	0.000 43	0.335 99	0.000 25	−4.9456	0.0037
2459.58949268	−25 951.90	2.95	7.2230	0.0059	51.780	0.042	−0.0467	0.0059	0.207 32	0.000 81	0.337 73	0.000 40	−4.9534	0.0058
2460.68089277	−25 942.78	2.17	7.2312	0.0043	51.747	0.031	−0.0484	0.0043	0.199 74	0.000 27	0.323 86	0.000 21	−4.9177	0.0033
2461.61328194	−25 950.89	2.38	7.2216	0.0048	51.758	0.034	−0.0482	0.0048	0.206 43	0.000 42	0.333 20	0.000 26	−4.9397	0.0040
2462.59779913	−25 952.54	2.76	7.2323	0.0055	51.768	0.040	−0.0544	0.0055	0.202 47	0.000 44	0.332 46	0.000 30	−4.9271	0.0050
2464.59168365	−25 943.37	6.05	7.2300	0.0121	51.681	0.087	−0.0550	0.0121	0.200 81	0.001 29	0.330 41	0.000 82	−5.0067	0.0196
2465.55365903	−25 950.80	2.57	7.2260	0.0051	51.679	0.037	−0.0511	0.0051	0.208 78	0.000 47	0.332 29	0.000 28	−4.9127	0.0043
2472.64517694	−25 941.76	3.16	7.2359	0.0063	51.753	0.045	−0.0520	0.0063	0.196 36	0.000 45	0.330 49	0.000 34	−4.9418	0.0068
2473.58292067	−25 943.18	4.22	7.2244	0.0084	51.761	0.061	−0.0520	0.0084	0.203 74	0.000 82	0.338 07	0.000 53	−5.0288	0.0123
2475.57164684	−25 941.40	2.96	7.2175	0.0059	51.614	0.042	−0.0479	0.0059	0.203 18	0.000 46	0.333 67	0.000 33	−4.8946	0.0055
2476.56363715	−25 940.68	2.08	7.2369	0.0042	51.694	0.030	−0.0435	0.0042	0.201 35	0.000 31	0.334 35	0.000 20	−4.9312	0.0032
2477.54328633	−25 943.82	2.36	7.2267	0.0047	51.619	0.034	−0.0477	0.0047	0.205 68	0.000 40	0.336 65	0.000 25	−4.9244	0.0039
2478.54019115	−25 942.74	2.84	7.2352	0.0057	51.520	0.040	−0.0336	0.0057	0.201 55	0.000 45	0.334 90	0.000 31	−4.8846	0.0049
2479.53140970	−25 947.93	2.57	7.2379	0.0051	51.599	0.037	−0.0496	0.0051	0.201 66	0.000 38	0.331 60	0.000 26	−4.9276	0.0046
2481.49463114	−25 946.30	3.03	7.2289	0.0061	51.619	0.043	−0.0492	0.0061	0.202 94	0.000 48	0.331 99	0.000 33	−4.9290	0.0060
2513.45063116	−25 941.24	2.40	7.2144	0.0048	51.895	0.035	−0.0373	0.0048	0.206 40	0.000 44	0.339 44	0.000 25	−4.9362	0.0047
2513.50299346	−25 947.17	3.03	7.2025	0.0061	51.855	0.044	−0.0382	0.0061	0.204 59	0.000 53	0.334 08	0.000 32	−4.9517	0.0073
2515.41998002	−25 948.56	2.34	7.2146	0.0047	51.939	0.034	−0.0431	0.0047	0.206 36	0.000 39	0.337 75	0.000 24	−4.9439	0.0045
2515.44534089	−25 950.25	1.94	7.2047	0.0039	51.950	0.028	−0.0464	0.0039	0.201 34	0.000 30	0.340 26	0.000 18	−4.9263	0.0032
2516.53158394	−25 947.31	3.15	7.2198	0.0063	51.853	0.045	−0.0425	0.0063	0.201 64	0.000 51	0.333 78	0.000 33	−4.9089	0.0073
2565.36730046	−25 946.28	1.77	7.2193	0.0035	51.900	0.025	−0.0456	0.0035	0.204 31	0.000 30	0.338 99	0.000 17	−4.9267	0.0028
2566.34623047	−25 947.65	2.17	7.2162	0.0043	51.897	0.031	−0.0510	0.0043	0.206 11	0.000 38	0.339 52	0.000 22	−4.9266	0.0039
2575.40577181	−25 940.30	2.32	7.1948	0.0046	51.938	0.034	−0.0472	0.0046	0.199 44	0.000 32	0.327 69	0.000 22	−4.9057	0.0044
2579.38604962	−25 941.06	2.55	7.2168	0.0051	51.803	0.037	−0.0471	0.0051	0.206 63	0.000 39	0.338 12	0.000 25	−4.9279	0.0054
2580.41346947	−25 943.54	5.80	7.2096	0.0116	51.886	0.084	−0.0440	0.0116	0.215 83	0.001 28	0.336 56	0.000 73	−5.0510	0.0261
2584.34061165	−25 943.38	3.56	7.2126	0.0071	51.855	0.051	−0.0389	0.0071	0.207 06	0.000 65	0.344 49	0.000 40	−4.9638	0.0099
2588.34564266	−25 941.61	5.73	7.2024	0.0115	51.732	0.082	−0.0406	0.0115	0.215 10	0.001 04	0.339 94	0.000 69	−5.1394	0.0308
2601.31755833	−25 939.58	2.08	7.2186	0.0042	51.878	0.030	−0.0441	0.0042	0.210 07	0.000 31	0.333 86	0.000 20	−4.8917	0.0033
3574.66373124	−25 937.49	2.73	7.2156	0.0055	51.803	0.039	−0.0596	0.0055	0.200 92	0.000 41	0.335 68	0.000 28	−4.9432	0.0058
3576.67067116	−25 940.31	4.33	7.1878	0.0087	52.058	0.063	−0.0508	0.0087	0.206 41	0.000 67	0.330 27	0.000 48	−4.9307	0.0123
3584.66117572	−25 952.06	3.29	7.2038	0.0066	51.971	0.047	−0.0413	0.0066	0.193 82	0.000 50	0.330 94	0.000 34	−4.9184	0.0078
3593.35139703	−25 946.50	2.43	7.2084	0.0049	51.952	0.035	−0.0482	0.0049	0.199 50	0.000 39	0.331 75	0.000 24	−5.0023	0.0057
3594.39633670	−25 951.08	1.96	7.2063	0.0039	51.962	0.028	−0.0478	0.0039	0.203 73	0.000 30	0.332 83	0.000 18	−4.9150	0.0031
3619.43182686	−25 954.25	2.15	7.2178	0.0043	51.955	0.031	−0.0551	0.0043	0.208 30	0.000 51	0.342 74	0.000 24	−4.9483	0.0039
3626.43584414	−25 955.03	2.33	7.2124	0.0047	51.913	0.034	−0.0462	0.0047	0.202 40	0.000 43	0.340 80	0.000 24	−4.9182	0.0041
3628.45057967	−25 947.93	4.67	7.1976	0.0093	51.703	0.067	−0.0418	0.0093	0.200 78	0.000 91	0.351 96	0.000 57	−4.9337	0.0133
3652.37335477	−25 940.45	2.96	7.2105	0.0059	51.918	0.043	−0.0457	0.0059	0.207 05	0.000 66	0.334 66	0.000 36	−4.9787	0.0067

Table B2. Prior parameter distribution for the calculation of the interior compositions of TOI-1422 c and TOI-1422 b, where we solve for atmospheric mass, the mass of the rocky interior (comprising core and mantle), and $Z_{\rm env}$ (the envelope metallicity).

Parameter	Prior range	Distribution
$M_{\rm atm}$	$(10^{-3}-10^{0.5}) * \mathrm{M}_{\oplus}$	Log-uniform
$M_{\rm core+mantle}$	$\mathcal{N}(M_{\rm p}, \sigma^2_{M_{\rm p}})$	Gaussian
Z	0.02−1.0	Uniform

This paper has been typeset from a TEX/LATEX file prepared by the author.